

CLOUD CORE COLLAPSE AND THE ROLE OF TURBULENT MAGNETIC RECONNECTION DIFFUSION

M. R. M. LEÃO¹, E. M. DE GOUVEIA DAL PINO¹,
R. SANTOS-LIMA¹, AND A. LAZARIAN²*Draft version September 11, 2012*

ABSTRACT

For a molecular cloud clump to form stars some transport of magnetic flux is required from the denser, inner regions to the outer regions of the cloud, otherwise this can prevent the gravitational collapse. Fast magnetic reconnection which takes place in the presence of turbulence can induce a process of reconnection diffusion. This paper continues our numerical study of this process and its implications. In particular, extending our earlier studies of reconnection diffusion in cylindrical clouds we consider more realistic clouds with spherical gravitational potentials (from embedded stars) and also account for the effects of the gas self-gravity. We demonstrate that within our setup reconnection diffusion takes place. We have also derived the conditions under which reconnection diffusion becomes efficient enough to make an initially subcritical cloud clump to become supercritical and collapse. Our results indicate that the formation of a supercritical core is regulated by a complex interplay between gravity, self-gravity, the magnetic field strength and nearly transonic and trans-Alfvénic turbulence. In particular, self-gravity helps reconnection diffusion and, as a result, the magnetic field decoupling from the collapsing gas gets more efficient compared to the case of an external gravitational field. We demonstrate that reconnection diffusion is able to remove magnetic flux from collapsing clumps, but only a few of them develop nearly critical or supercritical cores, which is consistent with the observations. Their formation is restricted to a range of initial conditions for the clouds as follows: thermal to magnetic pressure ratios $\beta \sim 1$ to 3, turbulent to magnetic energy ratios $E_{\text{turb}}/E_{\text{mag}} \sim 1.62$ to 2.96, and densities $50 < n < 140 \text{ cm}^{-3}$, when considering $M_{\star} \sim 25M_{\odot}$, implying total (gas+stellar) masses $M_{\text{tot}} \lesssim 120M_{\odot}$.

Subject headings: diffusion — ISM: magnetic fields — magnetohydrodynamics (MHD) — star: formation — turbulence

1. INTRODUCTION

It is well known that star formation occurs in dense globule-like regions inside giant molecular clouds (Blitz 1993; Williams et al. 2000). This is due to their low temperatures and high densities which help the gravitational force to overcome the outward forces which act to prevent collapse. However, in spite of all observational and theoretical efforts, it is not yet fully clear how these globules form stars.

Two key ingredients are known to be present in the clouds: magnetic fields and turbulence. On one side, the magnetic pressure gradient is an important agent working against the gravitational collapse of the gas (see Mestel & Spitzer 1956, Mestel 1965, Mouschovias 1991). The stability of a cloud supported by the magnetic pressure may be quantified by the mass-to-magnetic flux ratio, $M/\Phi \simeq N/B$, where M is the cloud mass, B is the magnetic field, and N is the column density. This ratio in principle defines to what extent a static magnetic field can support a cloud against gravitational collapse (e.g., Nakano & Nakamura 1978, Crutcher 1999, 2005a, Crutcher & Troland 2008, Heiles & Crutcher 2005, Falgarone et al. 2008). Considering an initially spherical cloud, the critical value of this ratio implies $B_{\text{cr}} \simeq 2.57 \times (N/10^{21} \text{ cm}^{-2}) \mu\text{G}$, for hydrogen gas. Zee-

man measurements suggest that the mass-to-magnetic flux ratios in molecular cloud cores are around 2.0 times larger than the critical value for which gravity and magnetic support balance each other (Crutcher 2008).

Turbulence is ubiquitous in interstellar medium³ and molecular clouds are part of the big cascade. Turbulence rules the structuring and fragmentation of the molecular clouds in all scales, and probably also plays an important role during the different phases of star formation (Mac Low & Klessen 2004; McKee & Ostriker 2007). The observation of broad line widths ranging from a few to more than 10 times the sound speed indicate that the turbulent motions are mainly supersonic to transonic in the molecular clouds. Turbulence is also roughly in equipartition with the magnetic fields in the interstellar medium and for this reason it is believed to be trans-Alfvénic (Elmegreen & Scalo 2004; Heiles & Troland 2005). In fact, the inferred ratio between turbulent and magnetic energy for the cold neutral interstellar gas is roughly $1.3 < E_{\text{turb}}/E_{\text{mag}} < 1.9$ (Heiles & Troland 2005). The formation of structures appears to be related to compression caused by the compressional motions associated with the turbulent cascade. The relation between compressible and incompressible parts of the cascade depends on the sonic and Alfvén Machs of the turbulent

¹ Instituto de Astronomia, Geofísica e Ciências Atmosféricas, Universidade de São Paulo, R. do Matão, 1226, São Paulo, SP 05508-090, Brazil

² Department of Astronomy, University of Wisconsin, Madison, WI 53706, USA

³ Turbulence spectra are measured in ionized component of the medium (see Armstrong et al. 1995, Chepurnov & Lazarian 2009) and neutral hydrogen (see Lazarian & Pogosyan 2000, Stanimirovic & Lazarian 2001, Chepurnov et al. 2010) and CO lines (see Padoan et al. 2006, 2009).

flow (Cho & Lazarian 2002, 2003). Even if the turbulence is globally strong enough for supporting the cloud against gravity (Klessen et al. 2000; Mac Low & Klessen 2004; Vázquez-Semadeni et al. 2005), compressible motions could also cause the collapse at small scales, by generating high density regions in both magnetized (Heitsch et al. 2001; Nakamura & Li 2005; Melioli & de Gouveia Dal Pino 2006; Leão et al. 2009) and non-magnetized medium (Klessen et al. 2000; Elmegreen & Scalo 2004). There are several candidate mechanisms for injection of turbulent energy inside a cloud. Internal sources include feedback from low-mass and massive stars. The latter in particular, can induce turbulence through intense ionizing radiation, winds, and supernovae explosions (SNe) (McCray & Snow 1979; Melioli & de Gouveia Dal Pino 2006; Melioli et al. 2006; Leão et al. 2009). External candidates also include SNe shocks (Wada & Norman 2001; Elmegreen & Scalo 2004; Melioli & de Gouveia Dal Pino 2006; Melioli et al. 2006; Leão et al. 2009) and the galactic spiral structure (Roberts 1969; Bonnell et al. 2006). All these processes seem to have power enough for explaining the structuring and kinematics of the ISM, and could generate the observed dispersion of the gas velocities (Kornreich & Scalo 2000). Less energetic sources of turbulence include proto-stellar jets and winds, expansion of HII regions, and magneto-rotational instability, but their relative importance is still uncertain (Joung & Mac Low 2006; Ballesteros-Paredes 2006; Mac Low 2009).

The exact role that turbulence and magnetic fields play on clouds collapse and star formation is still highly debated. An important question in this debate is that, under ideal MHD conditions, all the magnetic flux should be brought together with the collapsing material and then the magnetic field in a proto-star should be several orders of magnitude higher than the observed in T-Tauri stars. This is often referred as the "magnetic flux problem" (see Galli et al. 2006, Johns-Krull 2007, Santos-Lima et al. 2012). In order to solve this problem one has to consider diffusive mechanisms that can remove magnetic flux from a collapsing cloud and allow star formation, at least under some circumstances.

To address this problem of magnetic field diffusion both in a partially ionized ISM and in molecular clouds, researchers usually invoke the ambipolar diffusion (AD) mechanism. AD, which was first discussed in the context of star formation by Mestel & Spitzer (1956), has been extensively discussed since then (e.g., Spitzer 1968; Nakano & Tadamaru 1972; Mouschovias 1976, 1977, 1979; Nakano & Nakamura 1978; Shu 1983; Lizano & Shu 1989; Fiedler & Mouschovias 1992, 1993; Li et al. 2008; Fatuzzo & Adams 2002; Zweibel 2002). In principle, AD allows magnetic flux to be redistributed during the collapse of low ionization regions as the result of the differential motion between the ionized and the neutral gas. Recent advances in the theory, however, have been questioning the efficiency of this diffusion process in real systems. Several authors (Shu et al. 2006, Krasnopolsky et al. 2010, 2011) explored the accretion phase in low-mass star formation and concluded that there should exist an effective diffusivity about three orders of magnitude larger than the Ohmic diffusivity in order to allow an efficient magnetic flux transport to occur. They found that AD could work in principle, but only under special

circumstances, considering specific dust grain sizes (see also alternative views in Li et al. 2011). In other words, there is still no consensus if AD alone is high enough to solve the magnetic flux transport problem in collapsing flows.

Lately, we have been exploring a new mechanism for magnetic flux transport whose grounds were originally proposed by Lazarian (2005) which is based on the model of fast magnetic reconnection in Lazarian & Vishniac (1999). In the presence of magnetic reconnection magnetic fields are not any more frozen in⁴ and undergo the process which was termed reconnection diffusion (see also Lazarian 2011; Lazarian et al. 2012b; Santos-Lima et al. 2010; de Gouveia Dal Pino et al. 2011; 2012; Santos-Lima, de Gouveia Dal Pino & Lazarian 2012, Lazarian, Esquivel & Crutcher 2012). Note, that the problem we face in star formation with the magnetic field is not of *dissipation* of magnetic flux, where, indeed, ordinary resistivity is necessary, but of magnetic diffusion. The ideal non-diffusive MHD condition holds in the absence of magnetic reconnection, but when the latter is present, changes in the magnetic field topology occur. The model by Lazarian & Vishniac (1999) was confirmed by numerical high resolution MHD simulations (Kowal et al. 2009, 2012) and this provides the justification of our interpreting of our numerical results which do not provide as good resolution of current sheets as those in Kowal et al. studies. A detailed review of the theoretical foundations of this diffusion mechanism by turbulent reconnection is presented in the Appendix A.

The first numerical study of reconnection diffusion was performed in Santos-Lima et al. (2010; see also Lazarian et al. 2010; de Gouveia Dal Pino et al. 2011) where we explored numerically the role of turbulent reconnection on the transport of magnetic field flux from the central, denser regions of a molecular cloud to the outer regions. This study performed high-resolution three-dimensional (3D) MHD simulations of ISM clouds considering a central gravitational field provided by embedded stars. In the presence of turbulence, these simulations revealed a decrease of the magnetic flux-to-mass ratio with increasing density at the center of the gravitational potential caused by the transport of the magnetic flux to the outskirts of the cloud by turbulent reconnection diffusion. The comparison of these results with systems without turbulence and in these cases revealed no change in the magnetic-flux-to-mass ratio, as one should expect for ideal MHD systems. This was a further evidence that in the cases with turbulence the transport is due to reconnection diffusion. This effect was observed both when starting with equilibrium distributions of gas and magnetic field and when following the evolution of dynamically unstable (gravitationally collapsing) configurations. Thus the process of turbulent magnetic field removal is in principle applicable both to quasi-static subcritical clouds and collapsing supercritical ones. The increase of the gravitational potential, as well as the decrease of magnetization of the gas showed an increase of the segregation of the mass and magnetic flux in the saturated final state of those simulations, supporting the notion

⁴ The point of the violation of magnetic frozen in condition within turbulent plasmas is discussed in detail in Eyink, Lazarian & Vishniac (2011).

that turbulent diffusivity relaxes the magnetic field + gas system in the gravitational field to its minimal energy state. These results were also found to be insensitive to the numerical resolution. Tests made with resolutions of 128^3 , and 512^3 gave essentially the same results as those of 256^3 thus confirming the robustness of the results and the method.

The study above, however, assumed for simplicity clouds with cylindrical gravitational fields. We here perform 3D MHD high resolution numerical simulations considering more realistic subcritical clouds with central spherical gravitational potentials (due to embedded stars) and also account for the effects of self-gravity. Our results essentially confirm the results of the previous study above, but also reveal the conditions under which turbulent reconnection diffusion is efficient enough to make an initially subcritical cloud to become supercritical and collapse (see also de Gouveia Dal Pino et al. 2012).

In Section 2, we describe the setup and the numerical methodology that we employed for performing 3D MHD simulations of molecular cloud cores or clumps. In Section 3, we present the results of the diffusion of magnetic flux by turbulence considering molecular clouds with self-gravity and a central spherical gravitational potential. In Section 4, we discuss our results and compare them with previous works and observations, and in Section 5 draw our conclusions.

2. PHYSICAL SETUP AND NUMERICAL METHODOLOGY

The astrophysical environment we want to investigate in this work consists of an initially *subcritical* molecular cloud clump with a small group of embedded stars sustained by magnetic field and turbulence. Our goal is to examine, by means of three-dimensional MHD numerical simulations, the conditions under which the transport of magnetic flux by turbulent reconnection will allow the contraction of the self-gravitating gas to form a supercritical core. We also consider a few models without including self-gravity in order to compare with the previous study of Santos-Lima et al. (2010). In most of our numerical experiments, the system starts already out-of-equilibrium between gravity and the other forces. An initially spherical gas clump with a central gravitational potential that mimics a small group of embedded stars is put in the middle of a homogeneous magnetized background, then an initial contraction of the gas takes place for a short period of time (of the order of the free-fall time), after which due to the presence of the magnetic field and the turbulence injected, the system evolves more smoothly. As an example, Figure 1 shows the logarithmic density map of the central slice of model N2b (with no turbulence injected yet) right after an initial fast contraction and the injection of turbulence (~ 1.1 Myrs). The magnetic field configuration is superimposed to the density map.

We also present one test with the clump starting in magneto-hydrostatic equilibrium for comparison with the other models. (In this case, we actually started with a uniform density cloud, let it relax to the equilibrium and then injected turbulence).

Each system is simulated inside a cubic domain with periodic boundaries. Since a typical giant molecular cloud has several clumps the use of periodic boundaries

to model one of these clumps is appropriate. For the sake of simplicity, we employ an isothermal equation of state, with a single temperature for the whole system, which means that it radiates quite efficiently.

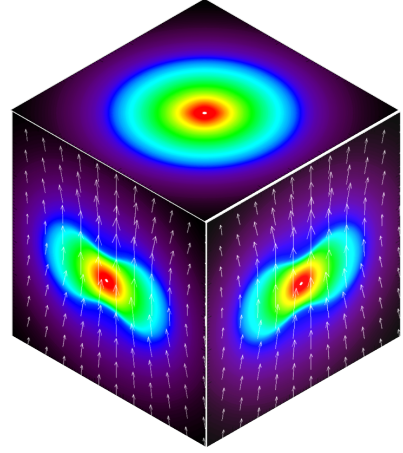


FIG. 1.— Example of a cloud setup in the computational domain (with no turbulence injected) right after an initial fast contraction at (~ 1.1 Myrs). Logarithmic density map and magnetic field lines of the central slice (projected onto the walls of the cubic computational domain) as in model N2b of Table 1 with $M_{pot} = 40.7 M_{\odot}$, initial density $n_0 = 90 \text{ cm}^{-3}$, and $\beta = 3.0$.

We chose characteristic values for the physical parameters of our models based on observational data (see, e.g. Mac Low & Klessen 2004)⁵. The computational domain has sides $L = 3.25 \text{ pc}$. For a grid resolution with 256^3 , the corresponding cell length is $\approx 0.013 \text{ pc} \sim 2600 \text{ AU}$. As remarked in Section 1, in the previous numerical study of 3D MHD turbulent reconnection diffusion in cylindrical clouds by Santos-Lima et al. (2010), tests with different resolutions between 128^3 , and 512^3 were performed and were found to produce essentially the same results, therefore in most of the simulated models here we considered a grid resolution of 256^3 (see however Fig. 9 below).

The isothermal sound speed is $c_s = 3 \times 10^4 \text{ cm/s}$, which corresponds to a temperature $T = 10.9 \text{ K}$ (for a mean molecular weight $\mu = 1.0$). In order to cover a parameter space as much appropriate as possible to the observed conditions we considered an initial uniform gas density, ρ_0 , spanning between $1.67 \times 10^{-23} \text{ g cm}^{-3}$ (or $n_0 = 10 \text{ cm}^{-3}$) and $1.67 \times 10^{-22} \text{ g cm}^{-3}$ (or $n_0 = 100 \text{ cm}^{-3}$). We have also considered values of the initial ratio between the thermal and the magnetic pressures, $\beta = c_s^2 \rho / (B^2 / 8\pi) = 3.0, 1.0$ and 0.3 . This implies initial Alfvén velocities $v_A \approx 2.4 \times 10^4 \text{ cm/s}$, $4.2 \times 10^4 \text{ cm/s}$, and $7.8 \times 10^4 \text{ cm/s}$, respectively, and initial uniform magnetic field intensities between $B_0 = 0.35 \mu\text{G}$ and $3.4 \mu\text{G}$.

The initial mass in stars in the cloud clump M_{\star} was also varied between $20\text{--}60 M_{\odot}$. They produce a spherical gravitational potential, $\Psi_{\star}(r)$, given by:

$$\Psi_{\star}(r \leq r_{max}) = -\frac{GM_{\star}}{(r + r_{\star})} \quad (1)$$

⁵ We note that in this study since we are considering self-gravity, the results are not scale independent, therefore, a physical parameter space must be considered

where r is the distance to the center of the computational box, and $r_{max} \sim 1.45\text{pc}$ is a cut-off in the gravitational force to ensure the symmetry while using periodic boundaries, and r_* is a smoothing radius. Its value gives the characteristic length of the clump. We fixed $r_* = 0.325\text{pc}$ in order to limit the values of the gravitational force and prevent the system to become Parker-Rayleigh-Taylor unstable.

In order to follow the evolution of the system we solve numerically the ideal MHD equations:

$$\frac{\partial \rho}{\partial t} + \nabla \cdot (\rho \mathbf{v}) = 0 \quad (2)$$

$$\rho \left(\frac{\partial}{\partial t} + \mathbf{v} \cdot \nabla \right) \mathbf{v} = -c_s^2 \nabla \rho + \frac{1}{4\pi} (\nabla \times \mathbf{B}) \times \mathbf{B} - \rho \nabla (\Psi_{gas} + \Psi_*) + \mathbf{f} \quad (3)$$

$$\frac{\partial \mathbf{B}}{\partial t} = \nabla \times (\mathbf{v} \times \mathbf{B}) \quad (4)$$

where the independent variables have their usual definition. The magnetic field \mathbf{B} , satisfies the divergence free condition $\nabla \cdot \mathbf{B} = 0$. The potential Ψ_{gas} is due to the gas self-gravity which obeys the Poisson equation:

$$\nabla^2 \Psi_{gas} = 4\pi G \rho \quad (5)$$

The source term \mathbf{f} of the second equation is the bulk force responsible for the injection of turbulence. We employ an isotropic, non-helical, solenoidal, delta correlated in time forcing f . It induces harmonic velocity fields isotropically distributed in the Fourier space, concentrated around a typical wavelength that defines the injection scale l_{inj} . The power supply is constant, keeping the random velocity of the gas v_{rms} approximately constant. In all our models with injection of turbulence, we use $l_{inj} \approx 1.3 \text{ pc}$ and v_{rms} between 2.4×10^4 and $5.7 \times 10^4 \text{ cm/s}$. The injection of turbulent energy starts at $t = 0.0 \text{ Myr}$ and grows slowly until it reaches its maximum at $t \sim 10.6 \text{ Myrs}$.

We employed a modified version of the Cartesian Godunov-MHD code originally developed by G. Kowal (Kowal et al. 2007; Falceta-Gonçalves et al. 2008; Santos-Lima et al. 2010), using the HLL solver and Runge-Kutta of second order for time integration. The Poisson equation is solved by a multigrid based algorithm (Press, Teukolsky & Flannery (1978)). The code is available upon request directly to the authors.

2.1. Initial Conditions

Table 1 shows the initial conditions for all the simulated models both with and without self-gravity. Models without self-gravity are labelled "R", the self-gravitating ones starting out of equilibrium are labelled "N" and the one starting in magneto-hydrostatic equilibrium is labelled "E" model. The "R" models, though scale independent, are also described here by their initial conditions in physical unities for comparison with the other models, except for the non-dimensional parameter A which measures the strength of the gravitational potential $A = (GM_*)/(Lc_s^2)$, where G is the Newton gravitational constant, M_* is the stellar mass potential, L is the

size of the computational domain (which also gives the distance unity in the code), and c_s is the sound speed (which is also the velocity unity in the code). The other parameters of the Table are the total mass M_{tot} , i.e., the sum of the mass in stars and the mass in gas, the initial cloud gas numerical density n_0 , the initial magnetic field B_0 , the thermal to magnetic pressure ratio β , the turbulent velocity v_{turb} , the Alfvénic velocity v_A , the initial cloud Jeans mass in the presence of magnetic field $m_{J,B}$, and the initial turbulent to magnetic energy density ratio E_{turb}/E_{mag} for the core ($r_c \leq 0.3\text{pc}$). The turbulent and Alfvén velocities are given in units of the isothermal sound speed $c_s = 3 \times 10^4 \text{ cm/s}$, which was chosen as the velocity unity in the code (see below).

Table 2 shows the dynamical time, $t_{dyn} = L/c_s$. This is compared with the free-fall time of the cloud gas which is given by,

$$t_{ff} = \sqrt{\frac{3\pi}{32 G \rho}} \quad (6)$$

and the reconnection diffusion time of the magnetic field, t_{diff} ,

$$t_{diff} = \frac{l^2}{\eta}, \quad (7)$$

where the turbulent reconnection diffusivity of the gas is (Santos-Lima et al. 2010; Lazarian 2006; 2011; Lazarian et al. 2012b):

$$\eta \sim l_{inj} v_{turb} \quad \text{if } v_{turb} \geq v_A, \\ \eta \sim l_{inj} v_{turb} \left(\frac{v_{turb}}{v_A} \right)^3 \quad \text{if } v_{turb} < v_A, \quad (8)$$

where $l_{inj} = L/k_f$ and $v_{turb} = v_{rms}$. The relations above indicate that the ratio $(v_{turb}/v_A)^3$ is important only in a regime of sub-Alfvénic turbulence, i.e. with the Alfvénic Mach number $M_A \leq 1$. In 7 above, l is the scale where the magnetic field is smoothed and is a fraction of the size of the computational domain L . In order to compare the models, in all simulations with turbulence we considered the same η (and therefore also the diffusion time). Thus for a given l , when changing β we also changed v_{turb} in order to keep η constant. This ensured that the turbulence decayed at approximately the same time scale in all models.

Also, in order to be able to detect the transport of magnetic flux during the dynamical evolution of the collapsing clouds, we made the initial turbulent reconnection diffusion time smaller than the initial free-fall time for all simulated models. We followed the evolution of B and ρ for at least ten time steps, corresponding to ten dynamical times, or in total $\sim 100 \text{ Myrs}$. For comparison with the turbulent MHD models, we also performed simulations with similar initial conditions but without injecting forced turbulence (these will be hereafter referred as "laminar" or non-turbulent models).

3. RESULTS OF THE NUMERICAL SIMULATIONS

3.1. Models with self-gravity

We present here the results for nine models where we have included the effects of self-gravity for which the ini-

TABLE 1
INITIAL CONDITIONS FOR THE MODELS

Model	$M_\star(M_\odot)$	A	$n_0(\text{cm}^{-3})$	$B_0(\mu\text{G})$	β	$v_{\text{turb}}(c_s)$	$v_A(c_s)$	$m_{J,B}(M_\odot)$	$E_{\text{turb}}/E_{\text{mag}}$
R1	61.1	0.9	10	0.35	3.0	0.8	0.8	373.7	2.96
R2	40.7	0.6	90	1.06	3.0	0.8	0.8	314.1	2.90
R3	27.1	0.4	100	1.12	3.0	0.8	0.8	326.6	2.89

Model	$M_\star(M_\odot)$	$M_{\text{tot}}(M_\odot)$	$n_0(\text{cm}^{-3})$	$B_0(\mu\text{G})$	β	$v_{\text{turb}}(c_s)$	$v_A(c_s)$	$m_{J,B}(M_\odot)$	$E_{\text{turb}}/E_{\text{mag}}$
N1	61.1	69.5	10	0.35	3.0	0.8	0.8	373.7	2.96
N2a	40.7	49.1	10	0.35	3.0	0.8	0.8	448.1	2.96
N2b	40.7	116.4	90	1.06	3.0	0.8	0.8	314.1	2.90
N2c	40.7	116.4	90	1.85	1.0	1.2	1.4	379.8	2.15
N2d	40.7	116.4	90	3.37	0.3	1.9	2.6	639.7	1.62
N2e	40.7	108.0	80	1.74	1.0	1.2	1.4	389.9	2.16
N3	27.1	111.2	100	1.12	3.0	0.8	0.8	326.6	2.89
N4	20.4	104.5	100	1.12	3.0	0.8	0.8	339.6	2.89
E1	40.7	46.6	90	1.06	3.0	0.8	0.8	390.1	2.90

TABLE 2
CHARACTERISTIC TIMESCALES.

Model	$t_{\text{dyn}}(\text{Myrs})$	$t_{ff}(\text{Myrs})$	$t_{diff}(\text{Myrs})$
R1	10.6	5.7	1.4
R2	10.6	4.4	1.4
R3	10.6	4.5	1.4
N1	10.6	5.7	1.4
N2a	10.6	6.7	1.4
N2b	10.6	4.4	1.4
N2c	10.6	4.4	1.4
N2d	10.6	4.4	1.4
N2e	10.6	4.5	1.4
N3	10.6	4.5	1.4
N4	10.6	4.6	1.4
E1	10.6	5.6	1.4

tial conditions are listed in Table 1. All models, but N2c, N2d, and N2e, have a turbulent velocity which is equal to the initial Alfvén speed, while these three models are sub-Alfvénic, i.e., have a turbulent velocity smaller than the Alfvén speed. The non-equilibrium models N1 and N2a were initialized with the same gas density $\rho = 1.67 \times 10^{-23} \text{g/cm}^3$, but different gravitational potentials (i.e., different values of the stellar mass potential M_\star). Model N2b has the same initial stellar potential as in model N2a, $40.7 M_\odot$, but a larger gas density $\rho = 1.503 \times 10^{-22} \text{g/cm}^3$ which allows to compare the effects of self-gravity. Models N2c and N2d have the same initial gas density as in the previous model, N2b, but different values of β which allow to compare the effects of the magnetic field. Model N2e has the same initial β as in model N2d but a slightly smaller gas density $\rho = 1.336 \times 10^{-22} \text{g/cm}^3$ which allows turbulence to be more dominant than in the previous case. The models N3 and N4 have the same initial $\beta = 3.0$ and gas density $\rho = 1.67 \times 10^{-22} \text{g/cm}^3$, but different stellar gravitational potentials, $27.1 M_\odot$ and $20.4 M_\odot$, respectively. Both have smaller stellar gravitational potentials but larger gas density (therefore more significant self-gravity) than the pre-

vious models. Finally, the model starting in equilibrium E1 has conditions which are similar to those of model N2b. The remaining initial conditions are the same for all models.

The left panels of Figures 2, 4, and 7, and top-left panel of Figure 6, show logarithmic density maps of the central slices of the simulated models after 100 Myr or \sim ten dynamical times. The middle panels compare the time evolution of the average magnetic field-to-density ratio inside a central sphere with radius $r = 0.3 \text{ pc}$ which represents the core of the cloud clump, $(\langle B \rangle_{0.3} / \langle \rho \rangle_{0.3}) / (\bar{B} / \bar{\rho})$, both for the models with turbulence (red-dashed line) and without turbulence (black-solid line). (The brackets mean averages taken inside the cloud radius 0.3 pc .) This ratio is normalized by the average value $(\bar{B} / \bar{\rho})$ taken over all the computational box. For the adopted geometry with an initial uniform magnetic field, the ratio above is approximately equal to the magnetic flux-to-mass flux ratio within the region considered.

The right panels of these figures and the top-right panel of Figure 6 depict profiles of the average magnetic field-to-density ratio as a function of the radial distance r from

the center of the cloud for the same models, at $t = 100$ Myr.

In Figure 2, we note that after an initial rapid decrease caused by the relaxation of the system, the magnetic field-to-density ratio inside the cloud cores (middle panels) remains nearly constant in the laminar cases (i.e., without turbulence), while in the cases with turbulence there is a clear decrease of it⁶. This result indicates that there was magnetic flux transport from the denser, more massive central regions to the less dense regions outside of the cloud cores. In Figure 2, this effect is particularly more pronounced in model N2b (bottom panel) which has much larger initial gas density than the other models of the Figure, and therefore is under the influence of larger self-gravity. Comparing models N1 and N2a which have the same initial gas density, we note that the one with larger stellar potential (model N1 in top panel) shows a larger decoupling between the magnetic flux and the mass density. Consistently, the right panels of Figure 2 show that the turbulent model with larger initial density (for which the effect of self-gravity is more important, i.e., model N2b), has a larger decrease in the radial profile of the magnetic field-to-density ratio in the core region (accompanied by a larger increase in the outer regions of the cloud) than the other turbulent models, therefore confirming the trend detected in the middle panels.

In order to verify if the initially subcritical clouds have developed supercritical cores after the action of the turbulent reconnection transport, Figures 11, 3, 5 and 8, and the bottom panels of Figure 6 compare the radial profiles of the integrated magnetic flux (left panels), mass (center panels), and mass-to-magnetic flux ratio normalized by the critical value (right), at $t = 100$ Myr for the models with and without turbulence⁷.

Figures 4 and 5 show the density maps and similar profiles as those of Figure 2 for the models with sub-Alfvénic turbulence N2c, N2d, and N2e. Models N2c and N2d have the same initial gas density and stellar mass as in model N2b, but smaller initial β and turbulent to Alfvén velocity ratio. This naturally makes the decoupling of the magnetic flux from the dense gas regions by turbulent reconnection diffusion more difficult. Both models N2c and N2d, for which $\beta = 1.0$, and 0.3 , respectively, have no significant magnetic flux transport outward when compared to model N2b in Figure 2 for which $\beta = 3.0$, or to their laminar counterparts. However, when the initial mass density of model N2c is decreased from 90 to 80 cm^{-3} (keeping $\beta = 1.0$), as in model N2e, the transport of magnetic flux by turbulence is slightly enhanced (though still much less than in model N2b) and the initially subcritical cloud develops a nearly critical core after 100 Myr (see Figure 5). Therefore, this result indicates that the increase of gas density and total gravity will not always result in enhancement of the flux transport by the turbulence as we have seen in the models of Figure 2. When turbulence is sub-Alfvénic

(and thus the magnetic field is strong for the level of turbulence applied), a smaller gravitational potential will delay the collapse and thus may give time for the turbulent reconnection diffusion to transport outward part of the magnetic flux. This explains why the decrease in density (and this of self-gravity) from $n_0 = 90 \text{ cm}^{-3}$ in model N2c to $n_0 = 80 \text{ cm}^{-3}$ in model N2e, results in the build up of a nearly critical core in the last case.

Figure 6 shows the density map and profiles for model E1. This model which starts in magneto-hydrostatic equilibrium has the same initial β and density ρ_0 in its central region as the non-equilibrium model N2b, but the equilibrium condition makes its density profile stratified and thus the total mass inside the cloud is smaller than in N2b model (see Table 1). As in the turbulent N2b model, E1 also suffers outward magnetic flux transport, as indicated by the decreasing magnetic field-to-density ratio in the core region (top-middle panel). However, the much smaller total mass of E1 prevents it to collapse and become a supercritical core, as indicated by the mass-to-magnetic flux diagrams of Figure 6 (bottom-right panels, red-dashed line).

Figures 7 and 8 show the results for models N3 and N4 which have the same initial $\beta = 3.0$ and gas density $n_0 = 100 \text{ cm}^{-3}$ (which are comparable with model N2b for which the initial gas density is only a factor 0.1 smaller), but different stellar gravitational potentials, $27.1M_\odot$ and $20.4M_\odot$, respectively (which are smaller than that of model N2b).

In both turbulent models we note a smaller decrease with time of the magnetic field-to-density ratio in the cloud core relative to model N2b (see middle panels of Figure 7), specially for the model with smaller stellar potential (N4). The inspection of the radial profile of the mass-to-magnetic flux ratio at $t = 100$ Myr for this model in Figure 8 shows that in fact, there is no transport of magnetic flux in this case. This occurs because of the combination of two effects. The larger magnetic field of model N4 relative to model N2b (see Table 1) makes it more difficult for the turbulence to decouple the magnetic flux from the denser material. At the same time, the smaller stellar gravitational well slows down the infall of matter to the center in model N4 (see Table 2), while the action of the turbulence helps to spread the gas against gravity (bottom left panel of Figure 8). Model N3 on the other hand, although with the same strength of magnetic field as model N4, it has a stellar potential large enough to push the core matter inwards while turbulence decouples the magnetic flux transporting it to the less dense regions, allowing the formation of a supercritical core (as we see in the upper panels of Figure 8).

3.2. Effects of Resolution on the Results

As remarked, all the numerical simulations presented above have been performed with a resolution 256^3 . In order to ensure that the results above are not being affected by numerical effects, we also ran one of the models (model N2e, Table 1) with increased and decreased resolutions. Fig. 9 compares the same quantity presented in Figure 4 (middle panel) for this model with resolutions 128^3 , 256^3 , and 512^3 . We do not observe significant difference between them. Thus, we can expect that the

⁶ We note that the oscillations observed in these plots (which are slightly stronger in the laminar models) are acoustic oscillations of the cloud due to the fact that the virialization time of these systems is larger than the simulated period.

⁷ The critical value of the mass-to-magnetic flux ratio for a disk shaped system is given by: $(2\pi G^{1/2})^{-1}$

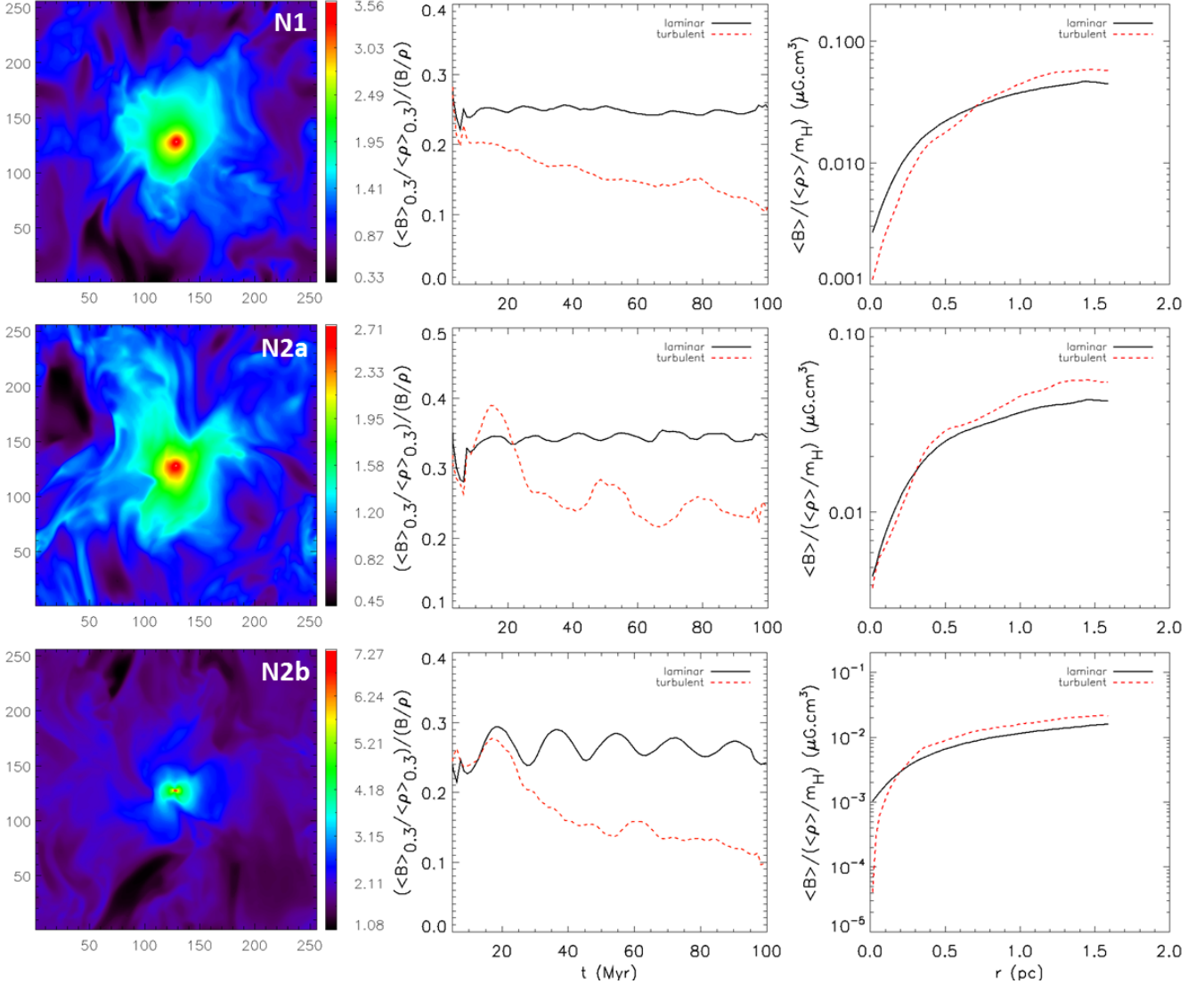


FIG. 2.— Model N1 with $M_{\text{pot}} = 61.1 M_{\odot}$ (top), models N2a (center) and N2b (bottom) with $M_{\text{pot}} = 40.7 M_{\odot}$. Top and middle models have initial densities $n_0 = 10 \text{ cm}^{-3}$, and the bottom model N2b has $n_0 = 90 \text{ cm}^{-3}$. All models have $\beta = 3.0$. Left panels show logarithmic density maps of the central slices of the turbulent cloud models at $t = 100$ Myrs. Middle panels show the temporal evolution of the average magnetic field-to-density ratio at the cloud core region of radius $r_c = 0.3$ pc normalized by the average value over the entire cloud, $((B)_{0.3}/\langle\rho\rangle_{0.3})/(\langle B\rangle/\langle\rho\rangle)$, for the turbulent (red-dashed lines) and the laminar (black continuous lines) models. Right panels show the radial profile of the average magnetic-to-density ratio at $t = 100$ Myrs $\langle B\rangle/\langle\rho\rangle$ for these models.

results presented for the models with resolution of 256^3 are robust.

3.3. Models with no self-gravity

We have not discussed yet the specific effects that the inclusion of self-gravity produces on the turbulent core collapse. In order to do that, we have to compare the self-gravitating models analyzed in the previous section with counterparts *without* self-gravity. These models labelled “R” are also listed in Table 1. Model R1 has similar initial conditions to those of the self-gravitating model N1 of Table 1, with a gravitational potential parameter $A = 0.9$ which is equivalent to a stellar mass of $61.7 M_{\odot}$. Models R2 and R3, in turn, have similar initial conditions to the self-gravitating models N2b and N3 of Table 1, with $M_{\star} = 40.7 M_{\odot} \rightarrow A = 0.6$, and $M_{\star} = 27.1 M_{\odot} \rightarrow A = 0.4$, respectively.

The logarithmic density maps at 100 Myrs as well as

all the related radial and time evolution profiles for these models are presented in Figures 10 and 11.

The comparison of the models without self-gravity R2 and R3 with the self-gravitating models N2b and N3, respectively (bottom panels in Figures 2 and 3 and upper panels in Figures 7 and 8) reveals the importance of the inclusion of self-gravity, particularly in model R2 which does not develop a supercritical core contrary to its self-gravitating counterpart (model N2b). On the other hand, model R1 (top panels in Figures 10 and 11) is not much affected by the elimination of self-gravity, as we can see when comparing with the self-gravitating model N1 (top panels of Figures 2 and 3). In this case the external gravitational potential due to the embedded stars is already very high and dominates the cloud collapse making self-gravity non-negligible only in a very small radius close to the center.

Model R1 is also comparable to the model D2 of

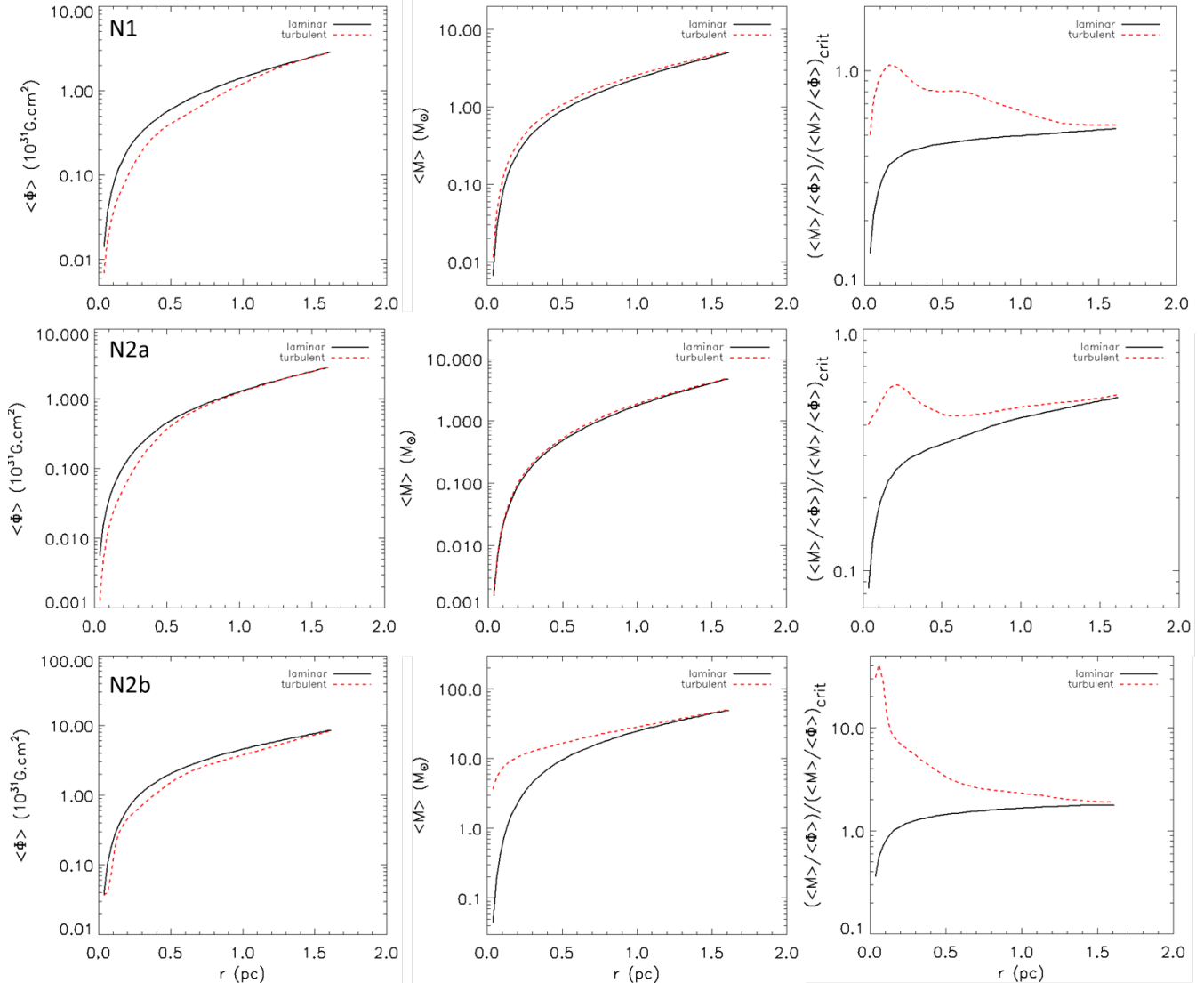


FIG. 3.— Radial profiles at $t = 100$ Myr for the magnetic flux Φ (left panels), the mass M (center panels), and for the magnetic flux-to-mass ratio normalized by the critical value $(M/\Phi)/(M/\Phi)_{crit}$ (right panels) for the models of Figure 2. Top panels: model N1 ($n_0 = 10 \text{ cm}^{-3}$, and $M_* = 61.1 M_\odot$); center panels: model N2a ($n_0 = 90 \text{ cm}^{-3}$, and $M_{pot} = 40.7 M_\odot$); bottom panels: model N2b ($n_0 = 10 \text{ cm}^{-3}$). Red-dashed lines are for turbulent models and black continuous lines are for the laminar models.

Santos-Lima et al. (2010). Both have the same initial conditions and no self-gravity, but differ in the geometry, as the clouds in Santos-Lima et al. have initial cylindrical gravitational potential rather than spheric. The presence of a spherical gravitational field yields a smaller efficiency in the magnetic flux transport, as we can see when comparing the top-middle diagram of Figure 2 with top-right panel of Figure 11 of Santos-Lima et al. (2010). This is because, while in the case of a spherical potential all matter is pushed to a single central point, in the case of a cylindrical potential, gravity pushes the collapsing material to the central axis all along the cylinder and thus it is more effective to help the decoupling between the collapsing gas and the magnetic flux driven by the turbulent reconnection diffusion.

4. DISCUSSION

We have performed 3D MHD simulations of the evolution of self-gravitating cloud clumps with a central gravitational potential with spherical symmetry and embed-

ded in an initially uniform magnetic field. For comparison we have also considered a few models without self-gravity. The simulations were started with the cloud either in magneto-hydrostatic equilibrium (see model E1 of Table 1) or out of it (all the other models of Table 1). We injected non-helical turbulence in each system with an rms velocity (v_{rms}) comparable both to the initial Alfvén speed and to the isothermal sound speed (see Table 1) and then let it to evolve. All the tested models have an initial turbulent to magnetic energy ratio > 1 , which is compatible with estimates from observations of the cold neutral interstellar medium (Heiles & Troland 2005). We have imposed to all systems the same turbulent time decay (eqs. 7) in order to compare the effects of the turbulent reconnection diffusion among them. Also for comparison, we evolved the same set of models with no injection of turbulence.

Most of the turbulent models here investigated evidence the transport of magnetic flux, i.e., the decoupling of the magnetic field from the denser, inner regions of

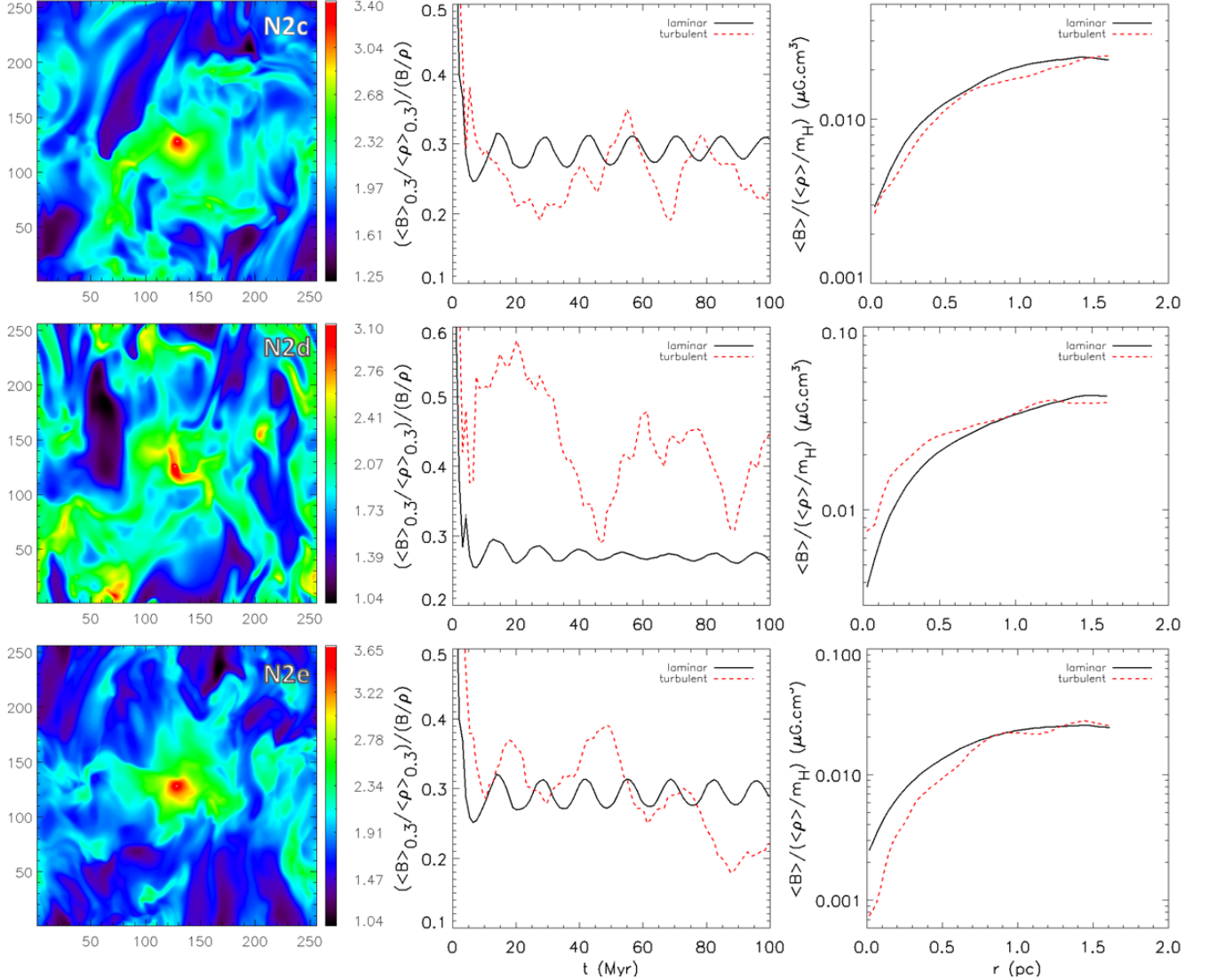


FIG. 4.— The same as in Figure 2 for models N2c, N2d, and N2e. Top and Bottom: models N2c and N2e with $\beta = 1.0$ Center: model N2d with $\beta = 0.3$. Top and middle models have initial densities $n_0 = 90 \text{ cm}^{-3}$, and the bottom model has $n_0 = 80 \text{ cm}^{-3}$. All models have $M_{\text{pot}} = 40.7 M_{\odot}$.

the cloud clump due to the presence of MHD turbulence. The exceptions are model R3 without self-gravity (as demonstrated by Figures 10 and 11) and the self-gravitating models N2c, N2d, and N4 (see Figures 4 and 5, and 7 and 8, respectively).

4.1. Comparison with Santos-Lima et al. (2010) results

Previous numerical studies of cylindrical cloud systems by Santos-Lima et al. (2010; see also Lazarian 2011; de Gouveia Dal Pino et al. 2011) had already evidenced the importance of the effects of turbulent magnetic reconnection to remove the magnetic flux excess from collapsing systems, as originally suggested by Lazarian (2005) based on the fact that magnetic reconnection must be fast in weakly MHD turbulent environments (Lazarian & Vishniac 1999; Kowal et al. 2009; see also Appendix A). The present numerical study, which considers more realistic self-gravitating spherical clouds, confirms the results of this previous analysis, i.e., it shows that the presence of turbulent reconnection diffusion is able to remove magnetic flux from the denser central regions to the edges

of the cloud, therefore facilitating the gravitational collapse in most of the tested models, without considering ambipolar diffusion effects. This is assured by the measured magnetic-flux-to-mass ratio in the core regions of the simulated clouds, which is quantified in our study by the average magnetic field-to-density ratio along the magnetic field lines (see middle diagrams of Figures 2, 4, 6-top, 7, and 10). This ratio decreases with time in most of the turbulent models, while it remains constant, on average, in the non-turbulent counterpart models.

As in Santos-Lima et al. (2010), we also find that, in general, an increase in the stellar gravitational potential (see e.g., models N1 and N2a of Figure 2), as well as a decrease in the initial magnetic field strength (or an increase in β ; see models N2b of Figure 2 and N2c and N2d of Figure 4) favours the turbulent reconnection transport of the magnetic flux and its decoupling from the dense collapsing gas.

In the cases when the turbulence is sub-Alfvénic (i.e., $v_{\text{turb}}/v_A < 1$, as in models N2c, N2d, and N2e), the flux transport by turbulent reconnection diffusion is more dif-

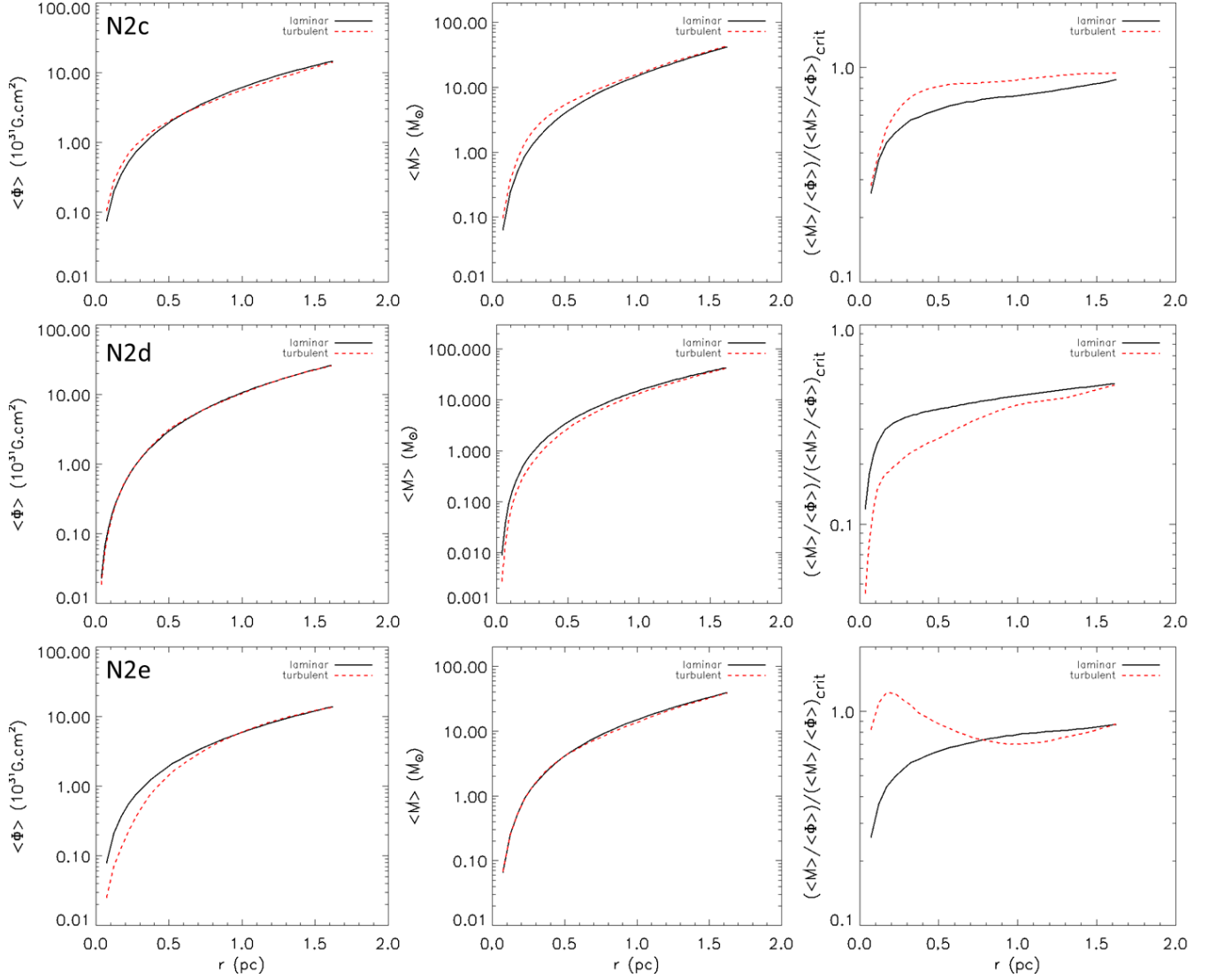


FIG. 5.— The same as in Figure 3 for models N2c, N2d, and N2e. Top panels: model N2c ($n_0 = 90 \text{ cm}^{-3}$, and $\beta = 1.0$); center panels: model N2d ($n_0 = 90 \text{ cm}^{-3}$, and $\beta = 0.3$); bottom panels: model N2e ($n_0 = 80 \text{ cm}^{-3}$, and $\beta = 1.0$).

ficult, as one should expect, since the turbulence at large scales is weak. In fact, for a cloud with an initially too large magnetic field, sub-Alfvénic turbulence will not be able to transport the magnetic flux to outside and the cloud may fail to build up a supercritical core, i.e., a core with a mass-to-magnetic flux ratio above the critical value that is required for gravity to overcome the magnetic forces (see for instance, models N2c and N2d in Figures 4 and 5 for which $\beta = 0.3$ and 1.0 , and $v_{\text{turb}}/v_A = 0.7$ and 0.9 , respectively).

Nonetheless, even sub-Alfvénic regimes of turbulence may allow the formation of critical cores. This was the case of model N2e, which has the same initial conditions of model N2c, except for a smaller total gravitational potential. The latter caused a delay of the gas collapse that gave time for the sub-Alfvénic turbulent reconnection, which becomes stronger at smaller scales (Lazarian 2006), to transport outward part of the magnetic flux and allow the formation of a critical core (see Figure 5).

This result can be understood in terms of the reconnection diffusion coefficient in sub-Alfvénic regimes. Al-

though weak at large scales, as the turbulence cascades the strength of the interactions increases and at a scale $l \simeq l_{\text{inj}}(v_{\text{turb}}/v_A)^2$ it becomes stronger and therefore, more efficient to help with magnetic flux transport. As stressed by Lazarian (2006, 2011) and also tested numerically by Santos-Lima et al. (2010), the diffusivity in this regime is expected to be given approximately by $l_{\text{inj}}v_{\text{turb}}(v_{\text{turb}}/v_A)^3$ (see eq. 8), thus smaller than the hydrodynamic turbulent diffusivity by a factor $(v_{\text{turb}}/v_A)^3$, with the eddies of the strong turbulence playing a critical role. In the next section we discuss the validity of this estimate for the turbulent reconnection diffusion coefficient.

4.2. Comparison of magnetic reconnection diffusivity and resistivity effects

As in Santos-Lima et al. (2010), we can evaluate the effective turbulent reconnection diffusion coefficient of our simulated models by comparing them with non-turbulent resistive models with enhanced Ohmic resistivity. For instance, considering the same initial condi-

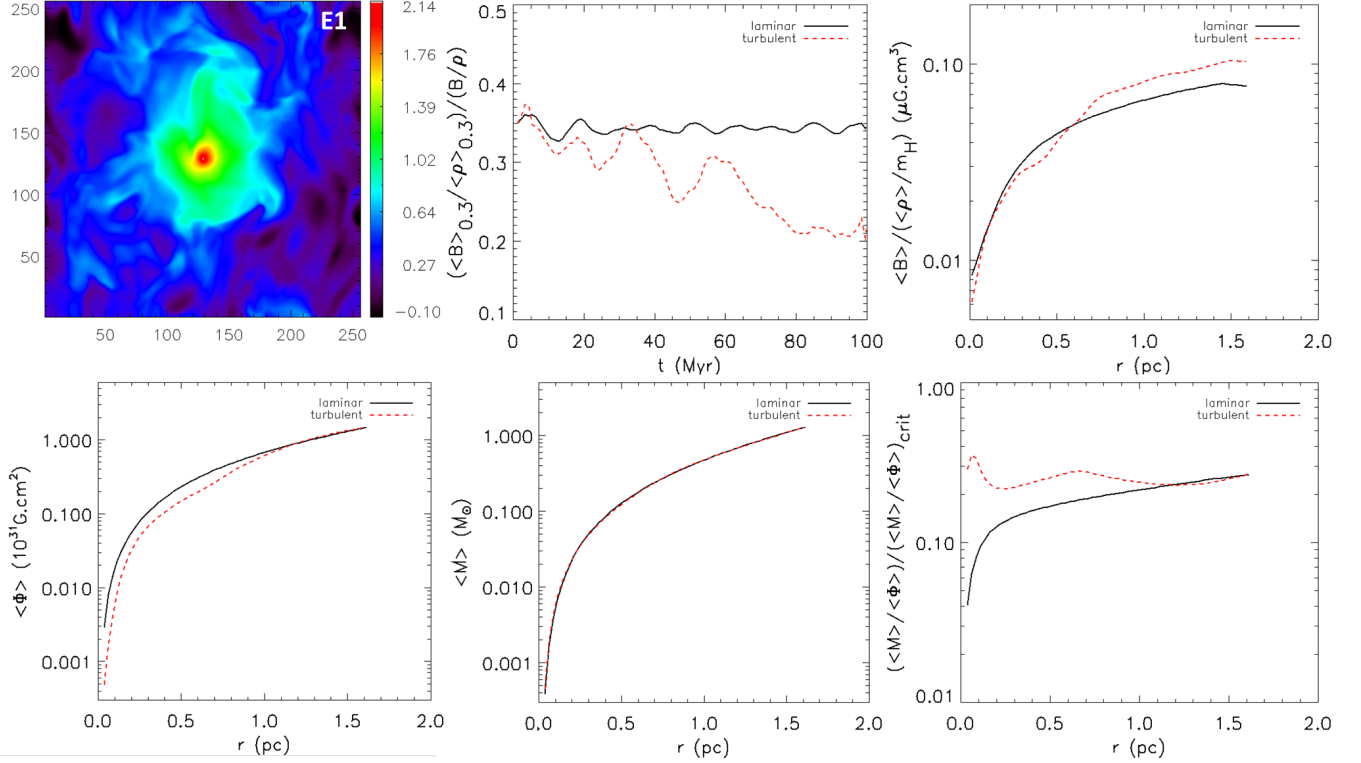


FIG. 6.— Equilibrium model E1 with $M_{\text{pot}} = 61.1 M_{\odot}$. This model has initial central density $n_0 = 90 \text{ cm}^{-3}$ and $\beta = 3.0$. Top: the same as in Figure 2 for model E1. Bottom: the same as in Figure 3 for model E1.

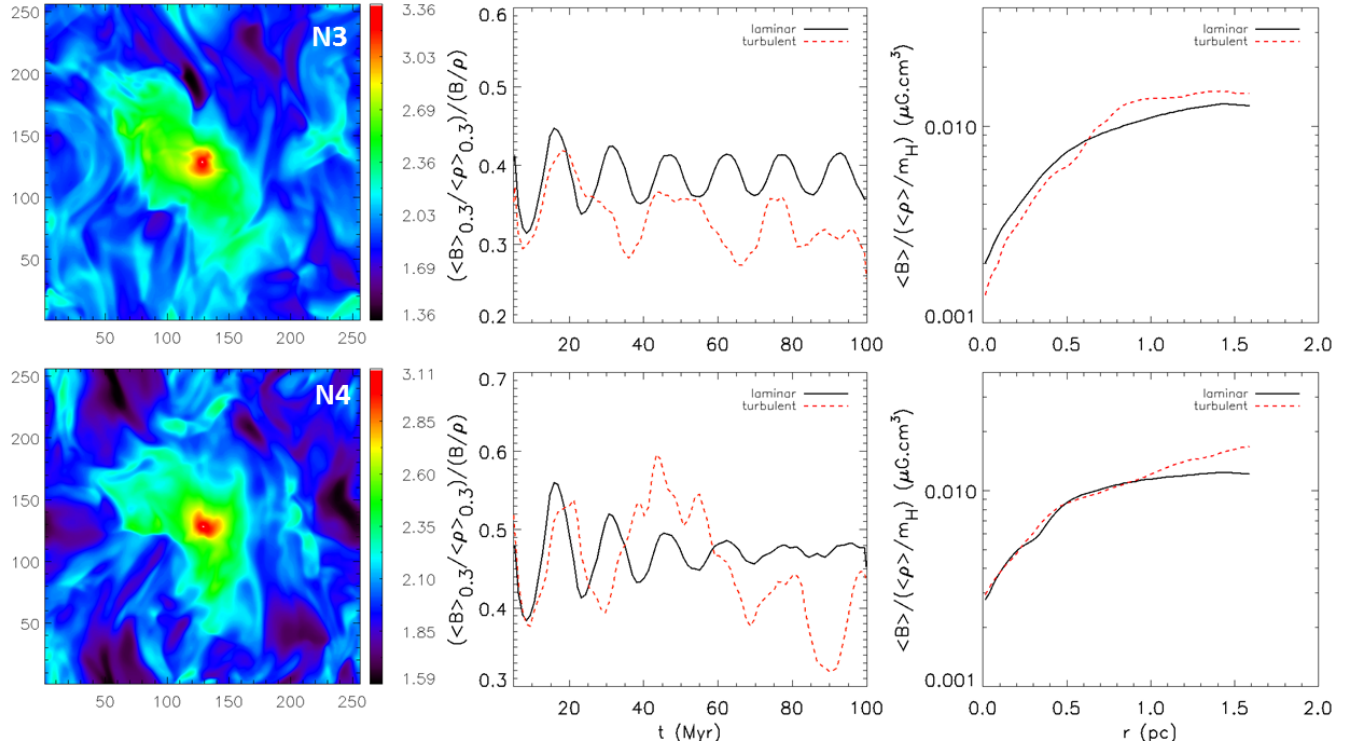


FIG. 7.— The same as in Figure 2 for the non-equilibrium models N3 and N4. Top: model N3 with $M_{\text{pot}} = 27.1 M_{\odot}$ bottom: model N4 with $M_{\text{pot}} = 20.4 M_{\odot}$. Both models have initial densities $n_0 = 100 \text{ cm}^{-3}$ and $\beta = 3.0$.

tions as those of the sub-Alfvénic models N2c, N2d and N2e, we performed several simulations of resistive non-turbulent models considering different values of Ohmic

resistivity. Table 3 presents a set of resistive models N2cr, N2dr, and N2er whose initial conditions are the same as those of N2c, N2d and N2e, respectively. Figure

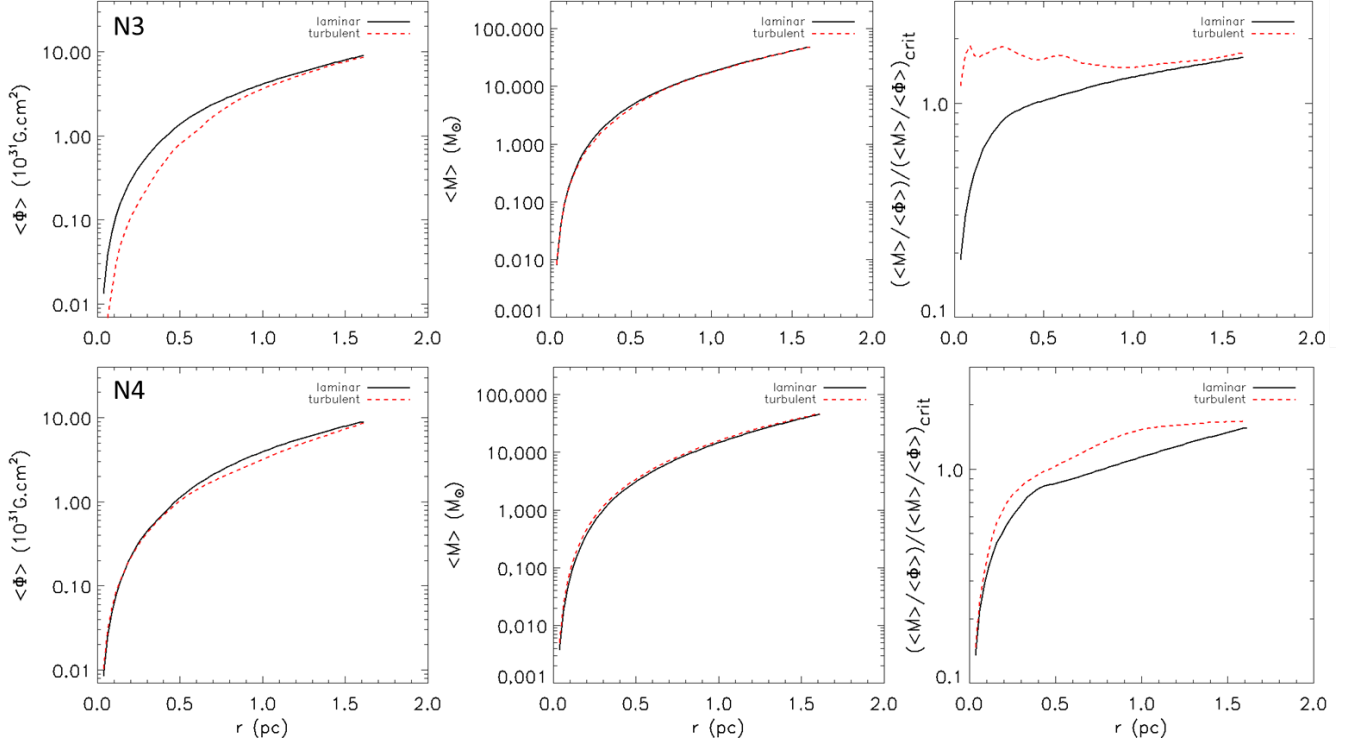


FIG. 8.— The same as in Figure 3 for models N3 and N4 of Figure 7. Top panels: model N3 ($n_0 = 100 \text{ cm}^{-3}$, and $M_{\star} = 27.1 M_{\odot}$); bottom panels: model N4 ($n_0 = 100 \text{ cm}^{-3}$, and $M_{\star} = 20.4 M_{\odot}$).

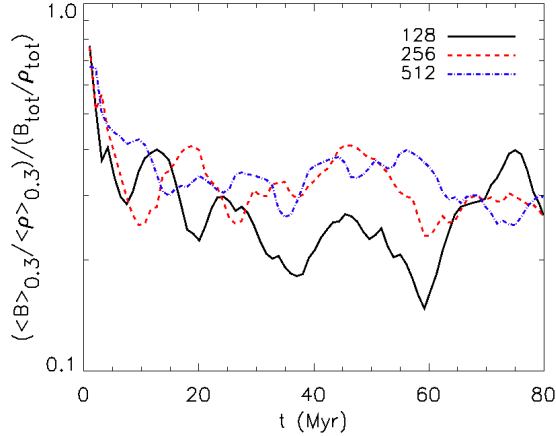


FIG. 9.— Comparison between different resolutions for the model N2c (Table 1).

12 compares model N2c with two resistive models N2cr1 and N2cr2 with same initial conditions and enhanced Ohmic resistivities $\eta_{Ohm} = 0.005 \text{ c.u.}$ and $\eta_{Ohm} = 0.001 \text{ c.u.}$, respectively. We see that the resistive model with $\eta_{Ohm} = 0.001$ is the one which best reproduces model N2c, thus we can conclude that the effective turbulent resistivity of model N2c is $\eta_{turb} \approx 0.001 \text{ c.u.}$ A similar procedure for models N2d and N2e allowed us to estimate also their turbulent diffusion coefficients, which are presented in Table 4. This Table also shows the corresponding upper limit estimates for the ratio $\eta_{turb}/l_{inj}v_{turb}$ (and the Alfvénic Mach number) for these models. According to eq. 8, we should expect this ratio to be smaller than 1 for sub-Alfvénic turbulence. Therefore, the obtained values are roughly consistent with the theoretical predic-

tions although further developments are still required in order to obtain a more precise values of the reconnection diffusion coefficients (see Lazarian 2011 and references therein).

TABLE 3
PARAMETERS FOR RESISTIVE MODELS WITH SAME INITIAL CONDITIONS OF THE SUB-ALFVÉNIC MODELS N2c, N2d AND N2e

Model	$n \text{ (cm}^{-3}\text{)}$	β	$\eta_{Ohm} \text{ (c.u.)}$
N2cr1	90.0	1.0	0.001
N2cr2	90.0	1.0	0.005
N2cr3	90.0	1.0	0.01
N2cr4	90.0	1.0	0.5
N2cr5	90.0	1.0	0.1
N2dr1	80.0	1.0	0.001
N2dr2	80.0	1.0	0.005
N2dr3	80.0	1.0	0.01
N2er1	90.0	0.3	0.0005
N2er2	90.0	0.3	0.001
N2er3	90.0	0.3	0.005

TABLE 4
THE DIFFUSIVITY COEFFICIENT FOR THE SUB-ALFVÉNIC MODELS

Model	$\eta_{turb} \text{ (c.u.)}$	$\eta_{turb}/v_{turb}l_{inj}$	$(v_{turb}/v_A)^3$
N2c	$\gtrsim 0.001$	$\gtrsim 0.0024$	~ 0.229
N2d	$\gtrsim 0.001$	$\gtrsim 0.0016$	~ 0.096
N2e	$\gtrsim 0.001$	$\gtrsim 0.0020$	~ 0.315

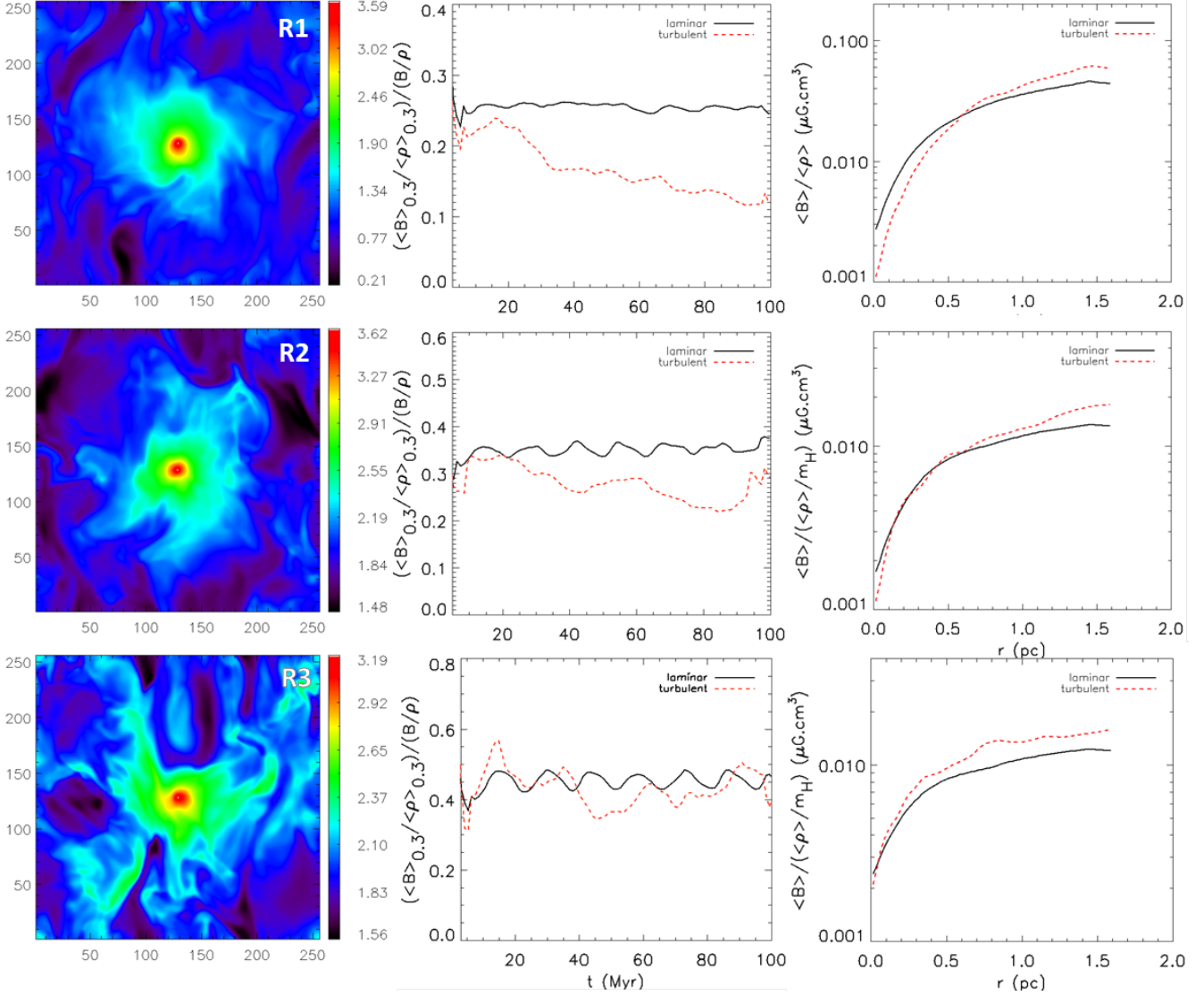


FIG. 10.— Model R1 with $A = 0.9$ ($M_{\text{pot}} = 61.1 M_{\odot}$) (top), model R2 (center) with $A = 0.6$ ($M_{\text{pot}} = 40.7 M_{\odot}$), and model R3 (bottom) with $A = 0.4$ ($M_{\text{pot}} = 27.1 M_{\odot}$). The models have initial densities $\rho_0 = 1.0$, and $\beta = 3.0$. Left panels show logarithmic density maps in the xz -plane of the central slices of the turbulent cloud models at $t = 100$ Myrs. Middle panels show the temporal evolution of the average magnetic field-to-density ratio at the cloud core region of radius $r_c = 0.3$ pc normalized by the average value over the entire cloud, $(\langle B \rangle_{0.3} / \langle \rho \rangle_{0.3}) / (\langle B \rangle / \langle \rho \rangle)$, for the turbulent (red-dashed lines) and the laminar (black continuous lines) models. Right panels show the radial profile of the average magnetic-to-density ratio at $t = 100$ Myrs $\langle B \rangle / \langle \rho \rangle$ for these models.

4.3. Cylindrical versus spherical gravitational potentials

Another result of particular importance here is the fact that in the presence of a more realistic spherical gravitational field in the cloud, the magnetic flux transport is less efficient than in the presence of a cylindrical field (as in Santos-Lima et al. 2010). This was already expected, since in a spherical potential all gas is pushed to a single central point, while in the cylindrical field the gas is pushed to the central axis along the cylinder making the decoupling of the gas from the magnetic flux, which is driven by the turbulent reconnection diffusion, more effective. Therefore, we may conclude that the results of the previous study based on cylindrical turbulent clouds by Santos-Lima et al. (2010) have overestimated the flux transport by reconnection diffusion. For instance, for model R1 with spherical potential (top panels of Figure 2) the normalized magnetic flux-to-density ratio has de-

creased by a factor 0.11 after 8 dynamical times, while the same model with cylindrical field in Santos-Lima et al. (2010) (model D2) has decreased by a larger amount, 0.65, at the same time interval.

4.4. Effects of self-gravity upon the magnetic flux transport by reconnection diffusion

The comparison of models without self-gravity with self-gravitating models have revealed that self-gravity can also significantly help the decoupling between gas and magnetic flux due to reconnection diffusion, particularly in the late stages of the cloud collapse. A critical example is the self-gravitating model N2b (Figures 2 and 3) in which reconnection diffusion causes the build up of a supercritical core, while its counterpart without self-gravity, model R2 (Figures 10), is unable to develop a supercritical core.

An increase of the self-gravity (which is provided by an

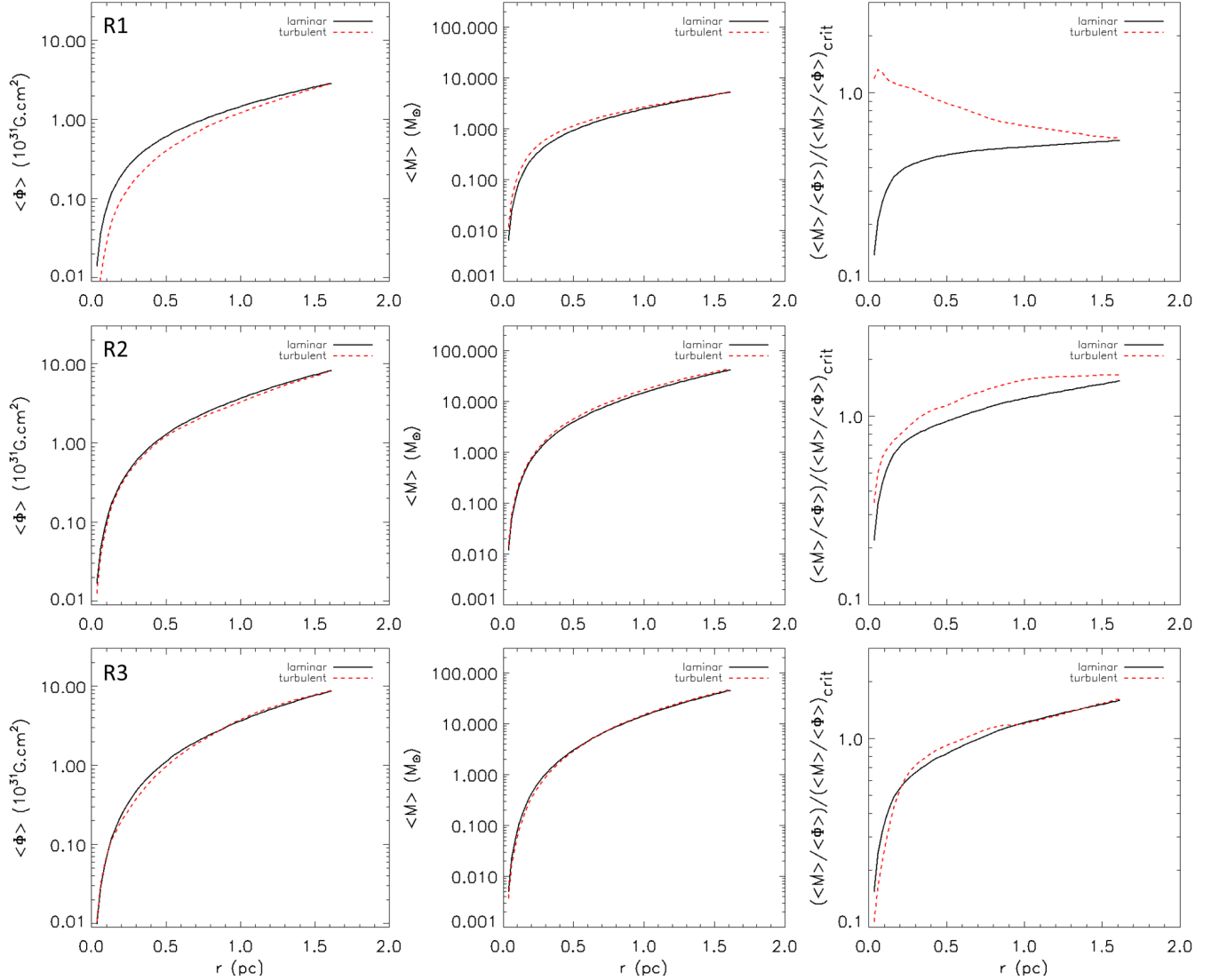


FIG. 11.— Radial profiles at $t = 100$ Myr for the magnetic flux Φ (left panels), the mass M (center panels), and the magnetic flux-to-mass ratio normalized by the critical value $(M/\Phi)/(M/\Phi)_{\text{crit}}$ (right panels) for the models of Figure 11. Top panels: model R1 ($A = 0.9$, i.e. $M_\star = 61.1 M_\odot$); center panels: model R2 ($A = 0.6$, i.e. $M_\star = 41.7 M_\odot$); bottom panels: model R3 ($A = 0.4$, i.e. $M_\star = 27.1 M_\odot$). Red-dashed lines are for turbulent models and black continuous lines are for the laminar models.

increase in the initial gas density of the cloud) improves the turbulent transport of the magnetic flux. If the gas density in the cloud is large enough ($n_0 > 50 \text{ cm}^{-3}$), its effect seems to be more important than that of the stellar gravitational potential (for $M_\star \sim 41 M_\odot$) to help the decoupling between the gas and the magnetic field (see models N2b and N3 in Figures 2 and 3 and 7 and 5). However, for a given strength of turbulence, if one increases the initial density or the stellar gravitational field indefinitely, then eventually the total gravitational potential will become so high that it will neutralize the ability of the reconnection diffusion to decouple the magnetic flux from the dense gas and thus, no efficient transport of magnetic flux will occur to outside of the cloud core, as most of it will be dragged by the infalling gas. We have seen this effect, for instance, when increasing the initial cloud density in model N2e (which has initial $\beta = 1.0$, $M_\star \sim 41 M_\odot$, and $n_0 = 80 \text{ cm}^{-3}$) to $n_0 = 90 \text{ cm}^{-3}$ in model N2c (see Figures 4 and 5). While the first model evidences some magnetic flux transport and

develops a nearly critical core, the second one fails completely. Similarly, for model N2b (which has $\beta = 3.0$, $M_\star \sim 41 M_\odot$, and $n_0 = 90 \text{ cm}^{-3}$), transonic, trans-Alfvénic turbulence allows the formation of a supercritical core, as indicated in Figures 2 and 3. However, if one increases its initial gas density to 100 cm^{-3} , the total gravitational potential becomes so large and makes the collapse so fast that the turbulent magnetic reconnection becomes ineffective to decouple the magnetic flux from the dense core. On the other hand, if one reduces the stellar mass of model N2b to $M_\star \sim 27 M_\odot$ and increases the gas density to 100 cm^{-3} as in model N3 (Figures 7 and 8), so that the total mass is nearly the same as in model N2b, then some flux transport is evidenced and a supercritical core develops, but a further reduction of the total mass (as in N4) again prevents the formation of a critical core, because in this case the infall becomes so slow that the turbulence actually helps to spread out the core material.

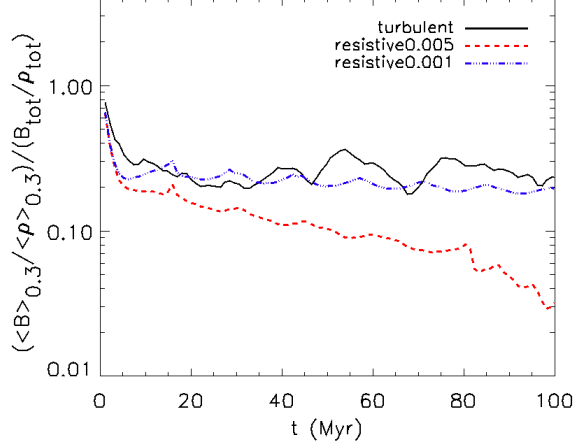


FIG. 12.— Temporal evolution of the average magnetic field-to-density ratio at the cloud core region within a radius $r_c = 0.3$ pc normalized by the average value over the entire cloud, for the turbulent N2e model (black, solid line), the resistive N2er1 model with $\eta_{ohm} = 0.001$ c.u. (blue, dot-dashed line); and the resistive N2er2 model with $\eta_{ohm} = 0.005$ c.u. (red, dashed line). We note that the resistive model N2er1 is comparable to the turbulent model N2e.

4.5. Effects of the cloud initial conditions

All the results above were found for cloud clumps which had initial uniform density and were out of magneto-hydrostatic equilibrium when turbulence was injected. We have also tested a model starting in magneto-hydrostatic equilibrium having a stratified density, with the central density and the remaining initial conditions as in our reference model (N2b) (see model E1 in Figure 6). As N2b, model E1 also undergoes an efficient outward magnetic flux transport due to turbulent reconnection. However, the much smaller total mass of E1 due to the cloud stratification (with a fraction 0.43 of the total mass of N2b model) prevents its collapse to form a supercritical core within the evolved time interval.

The results above indicate that the formation of a supercritical core is regulated by a complex interplay between gravity, self-gravity, the magnetic field strength and nearly transonic, trans-Alfvénic turbulence. Although we have found that turbulent reconnection diffusion is very efficient to remove magnetic flux from most of the collapsing core clump models tested here, only a few were succeeded to develop nearly critical or supercritical cores (see models N2b, N2e, and N3) which may be able to collapse and form stars. In other words, for the cloud conditions investigated here, the formation of supercritical cores is restricted to a limited range of parameters, as one actually should expect from observations that predict a low efficiency of star formation (see e.g. Mac Low & Klessen 2004; Leao et al. 2009; Vazquez-Semadeni et al. 2011).

To summarize, our results suggest that turbulent reconnection flux transport will allow initially sub-critical clouds to become nearly critical or supercritical for cloud clumps with initial values of $\beta \sim 1$ to 3, cloud densities $50 < n_0 < 100 \text{ cm}^{-3}$ when considering stellar masses $M_\star \sim 41 M_\odot$, and densities $100 < n_0 < 140 \text{ cm}^{-3}$ when considering stellar masses $M_\star \sim 27 M_\odot$, implying total cloud clump masses $M_{tot} \lesssim 120 M_\odot$. For smaller densities the clouds are fragmented by the injected turbulent

power and no core is build up⁸. For higher densities, the effects of self-gravity are so strong that the core collapses, dragging most of the magnetic field, so that no significant magnetic flux is detected. Of the 9 self-gravitating models here investigated, 4 formed marginally critical or supercritical cores (N1, N2b, N2e and N3) and 2 subcritical cores (N2a and E1), all of which evidenced turbulent magnetic flux transport. The 3 remaining models (N2c, N2d and N4) did not evidence any magnetic flux transport by reconnection diffusion (either because the initial cloud had too strong magnetic field or too strong turbulence, as described in Section 3). Table 5 lists the final conditions of the built up cores all simulated models.

4.6. Comparison of our results with observations

The direct approach to resolve the uncertainty concerning the process by which stars form is to measure the magnetic field strengths in molecular clouds in order to see whether they are weak enough (i.e., the cloud is supercritical) or strong (i.e., the cloud is subcritical). Recent Zeeman measurements of dark cloud cores and envelopes by Crutcher et al. (2009, 2010; see also Troland & Crutcher 2008) have raised new challenges to the current theory of magnetic flux transport by ambipolar diffusion. They obtained the mass-to-magnetic flux ratio between the cloud core and the envelope, $R = (M_c / \Phi_c) / (M_e / \Phi_e)$, as well as the mass-to-flux ratio between the core and the entire (core+envelope) cloud, $R' = (M_c / \Phi_c) / (M_{c+e} / \Phi_{c+e})$, and found that these ratios are less than unity for four observed clouds (B1, B217-2, L1448CO and L1544). The ambipolar diffusion requires the mass-to-magnetic flux ratio in the core to be larger than in the entire cloud, resulting $R' > 1$, which is in contradiction with the results found by Crutcher et al. Lazarian et al. (2012a) provided the explanation of the Crutcher et al. (2009) results that is based on the concept of reconnection diffusion. They, however, did not do numerical simulations and in their calculations relied on the phenomenological description of reconnection diffusion.

Although the conditions of the cloud core-envelopes investigated by Crutcher et al. are somewhat distinct from those obtained from the numerical simulations in the present study, we can make at least qualitative comparisons with their results. For instance, although denser and more magnetized, their cores are all subcritical or only marginally critical (i.e., they have mass-to-magnetic flux ratios relative to the critical value in the range $\mu_{crit} = 0.45 - 1.15$). The cores built up in our models which evidenced turbulent flux transport have final average mass-to-magnetic flux ratios $\mu_{crit} = 0.15 - 5.25$. Most of these cores have ratios R and R' which are consistent with the inferred ones by Crutcher et al. (2009), with the exception of the cores built up in models N1 and Nb2 (see Table 3, where these ratios are presented for the final snapshots of all our models). Indeed, observationally, it is known that the level of turbulence drops in the cores. We have seen that reconnection diffusion slows down with the decrease of the turbulent velocity (Santos-Lima et al. 2010; de Gouveia Dal Pino et al.

⁸ It is possible that this effect has been a little overestimated here due to the employment of an isothermal equation of state for the clouds.

2011; Lazarian 2011), so that as discussed in Lazarian et al. (2012a) we should expect a slower transport of magnetic flux to outside of the core as compared to the envelope. This behaviour is actually detected in the cores formed in the present study.

In the particular case of model N2b, the computed ratios R and R' are smaller than unity until the core becomes highly supercritical, from this point on R and R' become larger than unity due to the runaway increase of the mass-to-flux ratio of the collapsing core (maximum $\mu_{crit,c} \sim 40.7$, as shown in Table 5 and Figure 3).

Figures 13 and 14 illustrate the transport of the magnetic field lines from the collapsing core to the surrounding envelope for model N2b. While Figure 13 compares this turbulent model with its non-turbulent counterpart at the final snapshot ($t = 100$ Myr), Figure 14 depicts the time evolution of this turbulent model until the start of the core collapse around 90 Myr when then, the portion of the magnetic flux that was not diffusively transported to the surrounding envelope is advected to the center by the collapsing gas causing a large increase of the magnetic field intensity in this region.

In the case of model N1, the ratios R and R' are also smaller than 1 for several time-steps. After 68 Myrs, the very rapid increase of the central density caused by the high central gravitational potential in this model, makes R' and R to increase to values larger than 1 (the same situation applies to the non-self-gravitating model R1). Therefore, the three cores end up with R and $R' > 1$ because they are already collapsing to form proto-stars, N2b due to the dominance of self-gravity and N1 (and R1) due to the strong central potential. The other supercritical cores (N2e and N3) still have values of R and $R' < 1$ at the final snapshot, therefore comparable to those obtained for the observed cores by Crutcher et al.

We should note that the inferred values for R and R' from the observations are subject to significant uncertainties due to measurement limitations and simplified assumptions (see Mouschovias & Tassis 2010). Therefore, while encouraging, the results from the comparisons above should be viewed with caution. Besides, they call for further and more precise observational estimates of these ratios (see also Lazarian et al. 2012a).

5. CONCLUDING REMARKS

The mechanism here discussed of reconnection diffusion may present the last missing piece for constructing the new paradigm of star formation where turbulence and turbulent feedback play a central role (see also Lazarian 2011). The present numerical study together with the earlier one by Santos-Lima et al. (2010) have investigated this new mechanism focussing on the early stages of star formation. Recently, Santos-Lima et al (2012a, 2012b) have also investigated this mechanism in the late

stages, during the formation of the protostellar disks. These authors have shown, by means of 3D MHD simulations, that the diffusivity arising from magnetic reconnection in the presence of turbulence is also able to transport magnetic flux to the outskirts of the (cloud core) disk progenitor at time scales compatible with the core collapse. In just a few 10^4 yr, a rotationally supported disk forms around the protostar with a nearly Keplerian profile as required by the observations. Since MHD turbulence is expected to be present also in protostellar disks, this is a natural and fast mechanism for removing magnetic flux excess and allowing the formation of these disks. Therefore, taken together these studies have tested this new paradigm demonstrating that magnetic flux removal from molecular clouds by reconnection diffusion is very efficient and calls for reconsidering the relative role played by ambipolar diffusion (and other transport mechanisms) in the processes of star and planet formation.

Finally, we should remark that in this study, we have focused on the evolution of isothermal self-gravitating clouds with embedded stars which provided an external gravitational potential. As a matter of fact, some of the mentioned observed dark cloud cores contain stars embedded in them (e.g., B1 and L1448CO clouds; Bachiller, Menten, & del Rio-Alvarez 1990; Volgenau et al 2006). In forthcoming work, we will explore the effects of the magnetic flux transport by turbulent reconnection in the evolution of initially starless clouds in order to assess the effects of self-gravity only upon the transport, without considering an external field. Also, the isothermal approximation assumed here mimics the effects of an efficient radiative cooling of the gas. However, in more realistic cases, a detailed treatment of non-equilibrium radiative cooling in the clouds (e.g., Melioli et al. 2005) is required, particularly in the late stages of the core formation. The effects of non-equilibrium radiative cooling will be also considered in these forthcoming studies.

MRML acknowledges support from the Brazilian Agency CNPq (grants no. 140110/2008-9 and SWE 202114/2010-4), and EMGDP from the Brazilian agency FAPESP (grant no. 2006/50654-3) and CNPq (grant no. 300083/94-7). MRML also acknowledges the kind hospitality of A. Lazarian and his group during her three-month visit to the Astronomy Department of the University of Wisconsin. AL acknowledges NSF grant AST-1212096, Vilas Associate Award and the NSF Center for Magnetic Self-Organization in Laboratory and Astrophysical Plasmas. In addition, this study benefited from AL stay in the Universities of Cologne and Bochum enabled by the Humboldt Award as well as his stay at the International Institute of Physics (Natal, Brazil).

APPENDIX

THEORETICAL GROUNDS OF MAGNETIC FLUX TRANSPORT BY TURBULENT RECONNECTION

The magnetic diffusion mechanism that we address here is a process deeply rooted in the microphysics behavior of the magnetic fields in highly conductive flows. Textbooks characterize these flows by the Lundquist number $S = L_x v_A / \eta$, where η is the Ohmic diffusivity, L_x is a typical scale of the system and v_A is the Alfvén velocity. For astrophysical systems L_x is in general very large and therefore, $S \gg 1$ which makes magnetic diffusion negligible. However, one may ask: does the magnetic field remain absolutely frozen-in within highly ionized astrophysical fluids? The answer

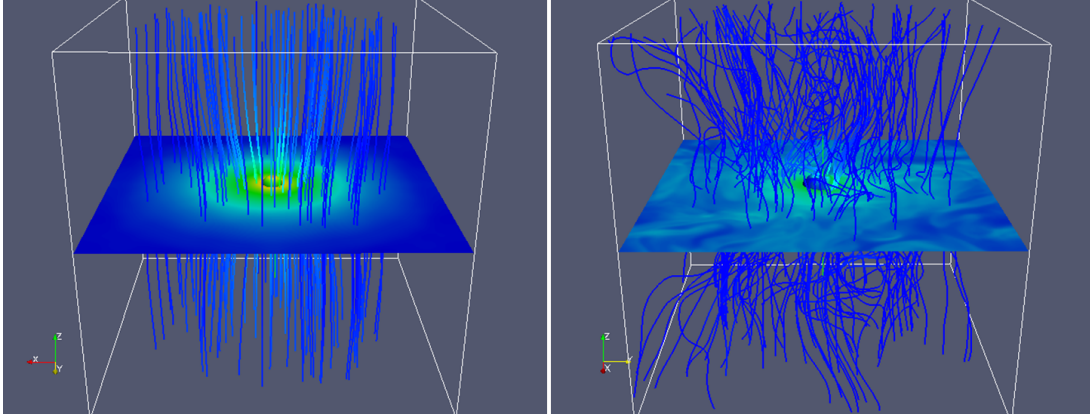


FIG. 13.— Magnetic field line distribution and the equatorial cut of the logarithmic density distribution for the collapsing cloud model N2b. The right panel shows the turbulent model while the left panel shows its laminar counterpart for comparison. The time depicted is 100 Myrs for both models. The central core has a density 50 cm^{-3} . 100 equally spaced magnetic field lines are plotted within a radius of $\sim 1.3 \text{ pc}$. The color scale indicates the intensity of the magnetic field with red representing the maximum and blue the minimum values.

TABLE 5

FINAL QUANTITIES OBTAINED FOR THE BUILT UP CORES AND ENVELOPES. CENTRAL DENSITY n_c AND MAGNETIC FIELD IN Z-DIRECTION B_c , TURBULENT-TO-MAGNETIC ENERGY RATIO E_{turb}/E_{mag} , MASS M_c , MAGNETIC FLUX Φ_c , AND MAXIMUM MASS-TO-MAGNETIC FLUX RATIO RELATIVE TO THE CRITICAL VALUE $\mu_{crit,c}$ FOR THE BUILT UP CLOUD CORES ($r_c \leq 0.3 \text{ pc}$). MASS M_e AND MAGNETIC FLUX Φ_e FOR THE FORMED CLOUD ENVELOPES; MASS-TO-MAGNETIC FLUX RATIOS BETWEEN THE CLOUD CORE AND THE ENVELOPE, R , MASS-TO-FLUX RATIOS BETWEEN THE CLOUD CORE AND THE ENTIRE CLOUD (CORE+ENVELOPE) CLOUD R' , AT THE FINAL TIME STEP ($t \sim 100 \text{ Myrs}$). MODELS N1, N2b, N2e, N3 AND R1 DEVELOPED SUPERCRITICAL OR marginally CRITICAL CORES. ALL MODELS BUT N2c, N2d, AND N4, EVIDENCED MAGNETIC FLUX TRANSPORT BY TURBULENT RECONNECTION DIFFUSION.

Model	$n_c(\text{cm}^{-3})$	$B_c(\mu\text{G})$	E_{turb}/E_{mag}	$M_c(M_\odot)$	$\Phi_c(10^{31}\text{G.cm}^2)$	$\mu_{crit,c}$	$M_e(M_\odot)$	$\Phi_e(10^{31}\text{G.cm}^2)$	R	R'
R1	3.8×10^3	1.92	4.83	0.7	0.20	1.32	7.7	3.54	1.52	1.47
R2	4.2×10^3	4.04	1.68	2.0	0.62	0.96	73.7	10.6	0.46	0.48
R3	994.7	3.32	3.55	1.1	0.43	0.73	83.0	11.2	0.33	0.34
N1	3.5×10^3	2.60	4.53	0.6	0.23	1.2	7.8	0.35	1.29	1.27
N2a	505.3	1.44	6.44	0.2	0.15	0.6	8.2	3.73	0.73	0.74
N2b	1.1×10^7	89.6	14.5	13.2	0.84	40.7	62.5	11.1	2.80	2.49
N2c	5.6×10^3	8.75	2.42	1.4	0.68	0.7	74.3	19.4	0.53	0.54
N2d	2.9×10^3	4.14	6.48	1.0	1.43	0.2	74.7	35.4	0.34	0.35
N2e	1.3×10^3	9.00	0.81	1.2	0.92	1.5	66.1	18.2	0.35	0.36
N3	2.3×10^3	3.79	7.72	1.7	0.31	2.0	82.4	11.8	0.79	0.79
N4	1.3×10^3	3.29	2.48	1.4	0.51	0.8	82.7	11.8	0.38	0.39
E1	111.6	0.85	0.77	0.1	0.11	0.3	2.2	1.93	0.39	0.41

to this question relies on magnetic reconnection.

Magnetic reconnection occurs when two magnetic fluxes of opposite polarity encounter each other. In the presence of finite magnetic resistivity, the converging magnetic lines annihilate at the discontinuity surface and a current sheet forms there. In the standard Sweet-Parker (S-P) model the velocity at which the two converging fluxes reconnect is given by $v_{rec} \approx v_A S^{1/2}$, where in this case L_x gives the length of the reconnection layer (see Figure 15). Because S is large for Ohmic resistivity values (e.g., for the ISM, $S \sim 10^{16}$), the Sweet-Parker reconnection is very slow. In other words, since all the matter moving with the speed v_{rec} over the scale L_x must be ejected with the Alfvén velocity through a thin slot (Δ), the disparity between the typical scales L_x and the outflow thickness Δ , which in turn is determined by microphysics, i.e. the resistivity, makes the Sweet-Parker reconnection rate negligibly small.

However, observations indicate that magnetic reconnection must be fast in some circumstances (e.g., solar flares). Lazarian & Vishniac (1999) proposed a model for fast reconnection that is independent of the resistivity. The model appeals to the ubiquitous astrophysical turbulence as a universal trigger of fast reconnection. When turbulence is present within the current sheet, the outflow region Δ gets determined by magnetic field wandering and therefore, becomes independent of the resistivity (see Figure 15, middle panel). It allows the formation of a thick volume filled with several reconnected small magnetic fluctuations which make the reconnection fast. This model was successfully tested numerically by Kowal et al. (2009) (see Figure 15, bottom panel). This challenges the well-rooted concept of magnetic field frozenness for the case of turbulent fluids and provides an interesting way of removing magnetic flux out of astrophysical flows, e.g. star formation regions (Lazarian 2005; Santos-Lima et al. 2010; 2012; de Gouveia Dal Pino et al. 2011), accretion disks, or the solar dynamo.

It must be remarked that numerical effects are always a concern when dealing with numerical simulations involving

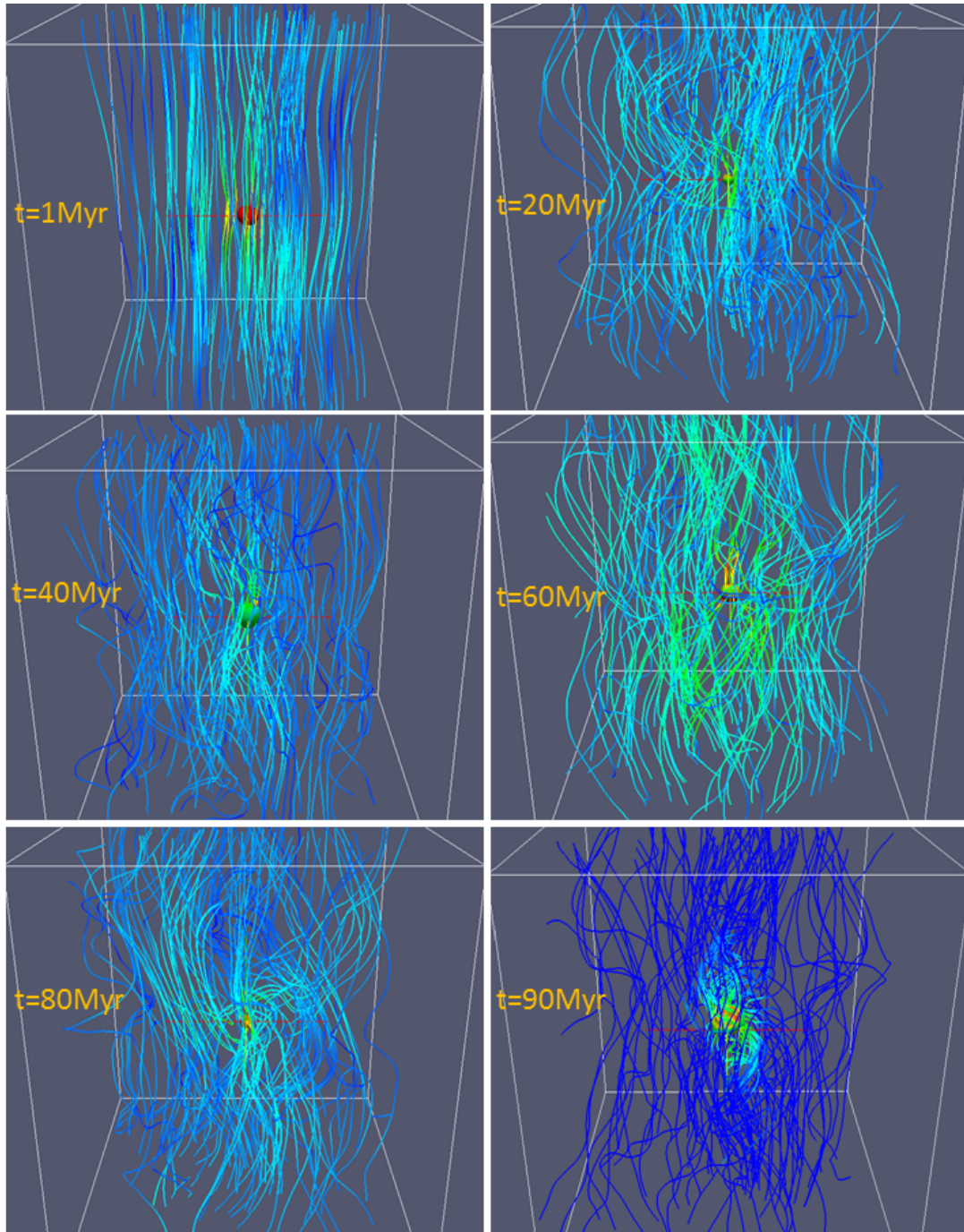


FIG. 14.— The same as in Figure 13, but showing the time evolution of the magnetic field lines of the turbulent model N2b from $t = 1$ to 90 Myr. We clearly see how turbulence diffusively transports the magnetic field lines as time evolves. At $t = 90$ Myr the lines that were not transported to the outskirts of the cloud are advected to the center by the collapsing gas causing a local enhancement in the magnetic field intensity.

reconnection and magnetic field diffusion. However, the high resolution numerical tests of magnetic reconnection performed by Kowal et al. (2009), showed that in the presence of turbulence the local non-linear enhancements of resistivity are not important. This is a confirmation that the turbulent reconnection diffusion that we observe in our simulations (see also Santos-Lima et al. 2010; 2012; de Gouveia Dal Pino et al. 2012) is a real effect and not a numerical artifact. Analytical studies summarized in Eyink et al. (2011) also support the notion that magnetic fields are generically not frozen-in when conductive fluids are turbulent. In view of these studies, we can conclude that the concept of reconnection diffusion looks very natural and ubiquitous.

REFERENCES

- Alves F. O., Girart J. M., Lai S.-P., Rao R., Zhang Q., 2011, *ApJ*, 726, 63
- Armstrong, J. W., Rickett, B. J., & Spangler, S. R. 1995, *ApJ*, 443, 209

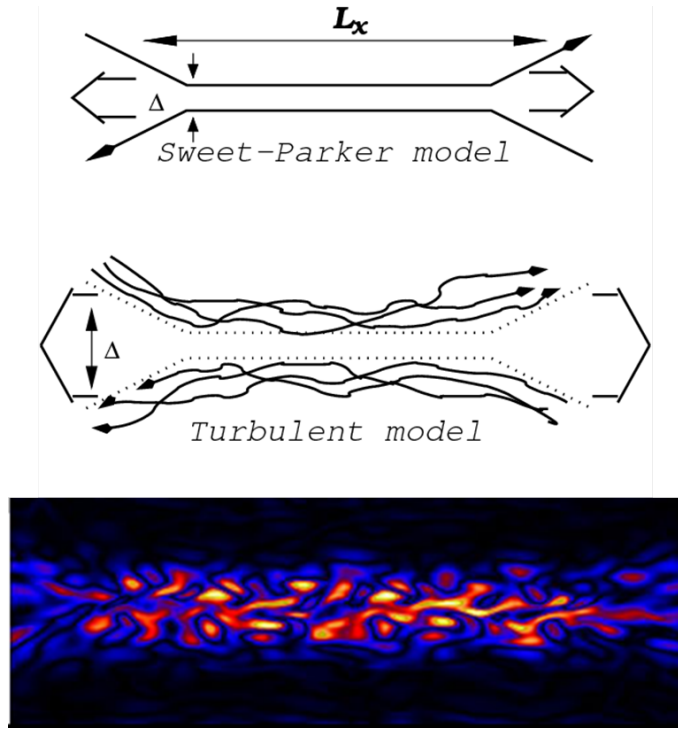


FIG. 15.— Top panel: the S–P model of reconnection. The outflow is limited by a thin slot Δ determined by Ohmic diffusivity. The other scale is an astrophysical scale $L_x \gg \Delta$. Middle panel: fast reconnection model in the presence of turbulence according to Lazarian and Vishniac (1999) (extracted from Lazarian et al 2004). Bottom panel: 3D MHD numerical simulation of fast turbulent reconnection (from Kowal et al. 2009). Modified from de Gouveia Dal Pino et al. 2012.

- Ballesteros-Paredes, J. 2006, MNRAS, 372, 443
 Biskamp, D. 1986, Physics of Fluids, 29, 1520
 Blitz, L. 1993, Protostars and Planets III, 125
 Bonnell, I. A., Dobbs, C. L., Robitaille, T. P., & Pringle, J. E. 2006, MNRAS, 365, 37
 Chepurnov, A., & Lazarian, A. 2010, ApJ, 710, 853
 Cho, J., & Lazarian, A. 2003, MNRAS, 345, 325
 Cho, J., & Lazarian, A. 2002, Physical Review Letters, 88, 245001
 Cho J., Lazarian A., Yan H., 2002, ASPC, 276, 170
 Crutcher, R. M. 1991, ApJ, 520, 706
 Crutcher, R. M. 1999, ApJ, 514, L121
 Crutcher, R. M. 2005, Massive Star Birth: A Crossroads of Astrophysics, 227, 98
 Crutcher, R. 2005, The Magnetized Plasma in Galaxy Evolution, 103
 Crutcher, R. M. 2008, Ap&SS, 313, 141
 Crutcher R. M., Troland T. H., 2007, IAUS, 237, 141
 Crutcher R. M., Hakobian N., Troland T. H., 2009, ApJ, 692, 844
 Crutcher R. M., Hakobian N., Troland T. H., 2010, MNRAS, 402, L64
 Crutcher, R. M., Wandelt, B., Heiles, C., Falgarone, E., & Troland, T. H. 2010, ApJ, 725, 466
 Elmegreen, B. G., & Scalo, J. 2004, ARA&A, 42, 211
 Falceta-Gonçalves, D., Lazarian, A., & Kowal, G. 2008, ApJ, 679, 537
 Falgarone, E., Troland, T. H., Crutcher, R. M., & Paubert, G. 2008, A&A, 487, 247
 Fatuzzo, M., & Adams, F. C. 2002, ApJ, 570, 210
 Fiedler, R. A., & Mouschovias, T. C. 1992, ApJ, 391, 199
 Fiedler, R. A., & Mouschovias, T. C. 1993, ApJ, 415, 680
 de Gouveia Dal Pino, E. M., Santos-Lima, R., Lazarian, A., Leão, M. R. M., Falceta-Gonçalves, D., & Kowal, G. 2011, IAU Symposium, 274, 333
 de Gouveia Dal Pino, E. M., Leão, M. R. M., Santos-Lima, R., Guerrero, G., Kowal, G., & Lazarian, A. 2012, Phys. Scr, 86, 018401
 Heiles, C., & Crutcher, R. 2005, Cosmic Magnetic Fields, 664, 137
 Heiles, C., & Troland, T. H. 2005, ApJ, 624, 773
 Heitsch, F., Mac Low, M.-M., & Klessen, R. S. 2001, ApJ, 547, 280
 Joung, M. K. R., & Mac Low, M.-M. 2006, ApJ, 653, 1266
 Klessen, R. S., Heitsch, F., & Mac Low, M.-M. 2000, ApJ, 535, 887
 Kornreich, P., & Scalo, J. 2000, ApJ, 531, 366
 Kowal, G., Lazarian, A., & Beresnyak, A. 2007, ApJ, 658, 423
 Kowal, G., Lazarian, A., Vishniac, E. T., & Otmianowska-Mazur, K. 2009, ApJ, 700, 63
 Krasnopolsky, R., Li, Z.-Y., & Shang, H. 2010, ApJ, 716, 1541
 Krasnopolsky, R., Li, Z.-Y., & Shang, H. 2011, ApJ, 733, 54
 Lada, C. J., & Lada, E. A. 2003, ARA&A, 41, 57
 Lazarian, A. 2005, Magnetic Fields in the Universe: From Laboratory and Stars to Primordial Structures., 784, 42
 Lazarian, A. 2006, ApJ, 645, L25
 Lazarian, A. 2011, arXiv:1111.0694
 Larazian, A., Esquivel, A., Crutcher, R. 2012, ApJ, in press, arXiv:1206.
 Lazarian, A., Eyink, G. L., & Vishniac, E. T. 2012, Physics of Plasmas, 19, 012105
 Lazarian, A., & Pogosyan, D. 2000, ApJ, 537, 720
 Lazarian, A., Santos-Lima, R., & de Gouveia Dal Pino, E. M. 2010, Numerical Modeling of Space Plasma Flows, Astronom-2009, 429, 113
 Lazarian, A., & Vishniac, E. T. 1999, ApJ, 517, 700
 Lazarian, A., Vishniac, E. T., & Cho, J. 2004, ApJ, 603, 180
 Leão, M. R. M., de Gouveia Dal Pino, E. M., Falceta-Gonçalves, D., Melioli, C., & Geraissate, F. G. 2009, MNRAS, 394, 157
 Lizano, S., & Shu, F. H. 1989, ApJ, 342, 834
 Mac Low, M.-M. 2009, Revista Mexicana de Astronomia y Astrofisica Conference Series, 36, 121
 Mac Low, M.-M., & Klessen, R. S. 2004, Reviews of Modern Physics, 76, 125
 McCray, R., & Snow, T. P., Jr. 1979, ARA&A, 17, 213
 McKee, C. F., & Ostriker, E. C. 2007, ARA&A, 45, 565
 Melioli, C., & de Gouveia Dal Pino, E. M. 2006, A, 445, L23
 Melioli, C., de Gouveia Dal Pino, E. M., de la Reza, R. & Raga, A. C. 2006, MNRAS, 373, 811
 Melioli, C., de Gouveia dal Pino, E. M., & Raga, A. 2005, A&A, 443, 495
 Mestel, L. 1965, QJRAS, 6, 265
 Mestel, L., & Spitzer, L., Jr. 1956, MNRAS, 116, 503

- Mouschovias, T. C. 1976, *ApJ*, 207, 141
Mouschovias, T. C. 1977, *ApJ*, 211, 147
Mouschovias, T. C. 1979, *ApJ*, 228, 475
Mouschovias, T. C. 1991, *ApJ*, 373, 169
Nakamura, F., & Li, Z.-Y. 2005, *ApJ*, 631, 411
Nakano, T. 1984, *Fund. Cosmic Physics*, 9, 139
Nakano, T., & Nakamura, T. 1978, *PASJ*, 30, 671
Nakano, T., & Tadamaru, E. 1972, *ApJ*, 173, 87
Parker, E. N. 1958, *ApJ*, 128, 664
Petschek, H. E. 1964, *NASA Special Publication*, 50, 425
Press, W. H., Teukolsky, S. A., & Flannery, B. P. 1992, *Numerical Recipes in Fortran 77: The Art of Scientific Computing.*, Vol.1, by William H. Press - 2nd. ed., Published by Press Syndicate of University of Cambridge, ISBN 0-521-43064-X.
Roberts, W. W. 1969, *ApJ*, 158, 123
Santos-Lima, R., Lazarian, A., de Gouveia Dal Pino, E. M., & Cho, J. 2010, *ApJ*, 714, 442
Santos-Lima, R., de Gouveia Dal Pino, E. M., & Lazarian, A. 2012a, *ApJ*, 747, 21
Santos-Lima, R., de Gouveia Dal Pino, E. M., & Lazarian, A. 2012b, *MNRAS*, submitted
Shay, M. A., Drake, J. F., Denton, R. E., & Biskamp, D. 1998, *J. Geophys. Res.*, 103, 9165
Shay, M. A., Drake, J. F., Swisdak, M., & Rogers, B. N. 2004, *Phys. of Plasmas*, 11, 2199
Shu, F. H. 1983, *ApJ*, 273, 202
Shu, F. H., Galli, D., Lizano, S., & Cai, M. 2006, *ApJ*, 647, 382
Stone, J. M., & Zweibel, E. G. 2010, *ApJ*, 724, 131
Strittmatter, P. A. 1966, *MNRAS*, 132, 359
Sweet, P. A. 1958, *Electromagn. Phenom. Cosm. Phys.*, 6, 123
Tassis, K., & Mouschovias, T. C. 2005, *ApJ*, 618, 769
Uzdensky, D. A., & Kulsrud, R. M. 2000, *Phys. of Plasmas*, 7, 4018
Vázquez-Semadeni, E., Kim, J., & Ballesteros-Paredes, J. 2005, *ApJ*, 630, L49
Vishniac, E. T., & Lazarian, A. 1999, *ApJ*, 511, 193
Wada, K., & Norman, C. A. 2001, *ApJ*, 547, 172
Williams, J. P., Blitz, L., & McKee, C. F. 2000, *Protostars and Planets IV*, 97
Yamada, M., Ren, Y., Ji, H., Breslau, J., Gerhardt, S., Kulsrud, R., & Kuritsyn, A. 2006, *Phys. Plasmas*, 13, 052119
Zweibel, E. G. 2002, *ApJ*, 567, 962